Calcium-intercalated molybdenum disulfide as electrocatalyst for carbon dioxide reduction

Master thesis

by

Songyan Liu

to obtain the degree of Master of Science
at the Delft University of Technology,
to be defended publicly on Wednesday, 26 April at 10:30

Student number:	5265940	
Project duration:	February 1, 2022 – April 26, 2023	
Supervisors:	Dr. Peyman Taheri	TU Delft
	Eszter Mádai	TU Delft
Thesis committee:	Dr. Yaiza Gonzalez-Garcia	TU Delft
	Dr. Prasad Gonugunta	TU Delft

TU Delft

Acknowledgements

Words cannot express my gratitude to people who helped me during the whole project. I am so lucky to enter this group and meet so many kind people here. Without their help, I couldn't finish my master thesis.

First, I'd like to thank my supervisors Dr. Peyman Taheri for his invaluable patience and support during the whole project. I also could not have undertaken this journey without my daily supervisor Eszter Mádai, who guided me to do experiments and gave feedback to my thesis. My special thanks to Khatereh Roohi for helping me with GC measurements. Additionally, this endeavor would not have been possible without the good suggestion of thesis committee. Prasad Gonugunta, in particular, made many good revisions to my thesis.

I am also grateful to technicians and student assistants, especially Agnieszka Kooijman for teaching me with lab works. Besides, I would like to say thanks to Mohammad Soleimani, Jasper Coppen, Yu Bi and all other people in the group. Thank you for sharing ideas with me and helping me with my experiments.

I went through a difficult time during my master's stage, and it was people's help that gave me the courage to keep going. Lastly, I would like to extend my sincere thanks to my family. Their encouragement kept my high motivation during my Master's study.

Abstract

In recent years, carbon dioxide and other greenhouse gases have been emitted on a large scale, leading to global warming, rising of sea levels, and causing many ecological problems. The use of fossil fuels is the chief source of large-scale emissions of CO_2, but the reliability and economy of fossil fuels make it difficult for other energy sources to replace it in a short time. Reducing CO_2 into other useful products like CO and CH_4 is a potential solution. The electrochemical methods stand out in the field of CO_2 reduction due to its mild and controllable conditions and the utilization of renewable source of energy. Design of efficient catalysts are essential for the electrochemical reduction of CO_2. Transition metal dichalcogenides, such as MoS_2 with high selectivity, low overpotential, and tunable structure is a potential candidate for catalysts. However, its performance still need to improve. The aim of this thesis us to develop a catalyst for CO_2RR. As the intercalation of ions increases the conductivity of MoS_2, the intercalation process of Ca^{2+} ions into MoS_2 was studied. Furthermore, how the newly engineered material performs in the CO_2RR was investigated.

In this study, two types of MoS_2, namely pristine MoS_2 and MoS_2 intercalated with Ca^{2+} ions were used. The Linear sweep voltammetry (LSV), Electrochemical Impedance Spectroscopy (EIS) and Chronoamperometry (CA) were used to examine the electrochemical performance. Their CO_2 reduction reaction performance in the $KHCO_3$ aqueous solutions was investigated by gas chromatography (GC), high pressure liquid chromatography (HPLC), and Nuclear Magnetic Resonance spectroscopy (NMR). The catalysts were characterized before and after the intercalation process using scanning electron microscopy (SEM), energy-dispersive X-ray spectroscopy (EDS), X-ray Diffraction (XRD), and X-ray photoelectron spectroscopy (XPS).

Keywords: CO_2 reduction reaction, transition metal chalcogenides, molybdenum disulfide, intercalation.

Acronyms

2D	Two-Dimensional
3D	Three-Dimensional
AM	Active Material
CA	Chronoamperometry
CB	Carbon Black
CO_2RR	CO_2 Reduction Reaction
CV	Cyclic Voltammetry
DI	Deionized
EDL	Electrical Double Layer
EDS	Energy Dispersive Spectroscopy
EIS	Electrochemical Impedance Spectroscopy
FE	Faraday Efficiency
FID	Flame Ionization Detector
GC	Gas Chromatography
HER	Hydrogen Evolution Reaction
HPLC	High Pressure Liquid Chromatography
IHP	Inner Helmholtz Plane
ILs	Ionic Liquids
IPA	Isopropanol
LSV	Linear Sweep Voltammetry
NMR	Nuclear Magnetic Resonance
OER	Oxygen Evolution Reaction
OHP	Outer Helmholtz Plane
PVA	Polyvinyl Alcohol
RHE	Reversible Hydrogen Electrode
SCE	Saturated Calomel Electrode
SEM	Scanning Electron Microscopy
SHE	Standard Hydrogen Electrode
TCD	Thermal Conductivity Detector
TMDs	Transition Metal Dichalcogenides
XPS	X-ray Photoelectron Spectroscopy
XRD	X-ray Diffraction

Contents

List of Figures

List of Tables

1

Introduction

1.1. Background

In recent centuries, as people entered the industrial society, carbon dioxide and other greenhouse gases have been emitted on a large scale, which causes the CO_2 concentration in the air to be unable to maintain balance through photosynthesis in nature [1]. The emission has directly led to the increase in the temperature of the earth's surface (Figure 1.1). Globally, 2011 to 2020 was the warmest decade on record [2]. Compared to the average temperature of the last century, this decade the temperature increased by 0.82 ^{o}C [3]. By the end of the century, average global temperatures are expected to be about 4 ^{o}C higher than they are today [4]. Polar glaciers are melting in this gradually warming environment, rising sea levels, which would submerge islands and land near the sea [5]. Extreme weather such as ocean storms would occur frequently. Some species' habitat destroyed by global warming, the environment they are living changes rapidly. These factors put many species at risk of extinction. This reduction of biodiversity could pose a threat to the ecological balance [6].

There are several different solutions to solve above mentioned problems. For example, reducing CO_2 emissions. Since fossil fuels are the main source of CO_2 emission, people can use solar power, wind power and other clean energy power with less environmental impact instead of fossil energy power [7]. However, fossil fuels are quite reliable and excepted to account for the largest proportion of energy use in the coming decades [8]. Current renewable energy harvesting devices have high cost and low efficiency, which limit their usage [7]. The other solution is converting CO_2 into useful products. Biochemical, electrochemical, photochemical, radiochemical, and thermochemical methods are potential methods to convent CO_2 [9]. Among these approaches, electrochemical methods with mild operation conditions is very attractive, due to its high efficiency and the possibility to use green energy in the process [10]. With the help of materials like copper, sliver, gold, graphene, and transition metal dichalcogenide, CO_2 can be reduced to hydrocarbons, CO and other value-added fuels and chemical feedstock.

However, electrochemical CO_2 reduction method still face some challenges. Firstly, the Hydrogen Evolution Reaction (HER) will compete with CO_2 reduction reaction, which results in the suppression of the CO_2RR. Secondly, CO_2 molecule is very stable, whose chemical bond need much energy to break. Also, The low solubility of CO_2 in the electrolyte also negatively affects the CO_2 reduction reaction [11]. The existing catalysts still face the problem of low selectivity, the obtained products are complex and diverse mixtures, which cause troubles for subsequent separation and application. The durability of the catalyst also needs to be improved [11].

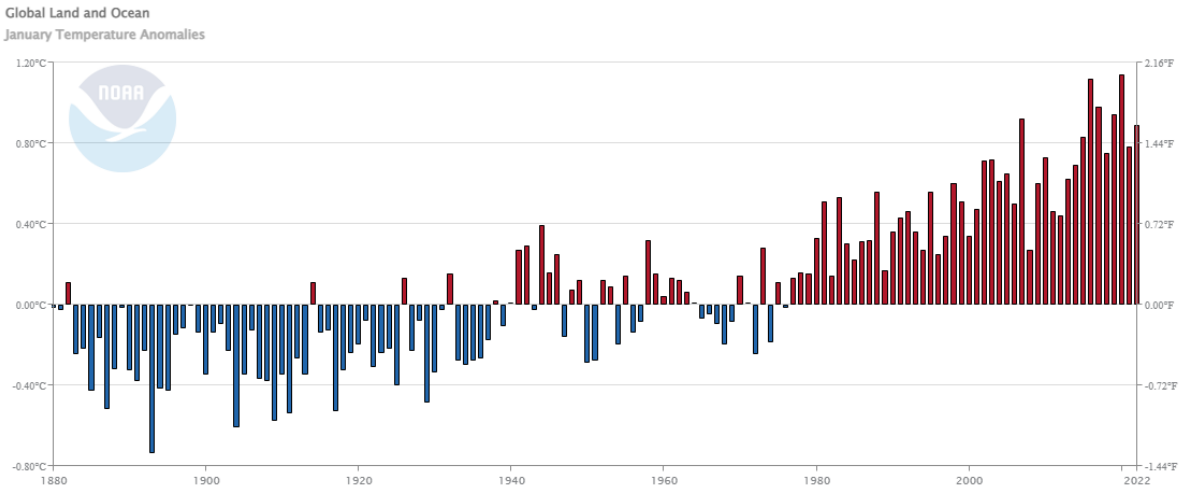

Figure 1.1: Annual Global (Land & Ocean) January Temperature Anomaly. Compared with the past decades, the global temperature has a clear upward trend [3].

Therefore, more effective catalyst need to be developed. The carbon capture methods are also need to be developed to be more efficient, existing CO_2 compression and transport technologies are still immature. Research on low-cost CO_2 adsorbents and their use in the large-scale is one of the solution [12].

Among the many reported materials, Group 6 transition metal dichalcogenides (TMDs) are very promising catalyst materials. TMDs, most notably molybdenum disulfide (MoS_2), molybdenum diselenide ($MoSe_2$), molybdenum ditelluride ($MoTe_2$), tungsten disulfide (WS_2) and tungsten diselenide (WSe_2) are thermodynamically stable layered materials [13]. They have high mobility values for electrons and holes. Due to their 2D structure, they can be made into nanosheets, nanotubes and quantum dot nano-objects. Due to the layered crystal structure, intercalation of different ions is possible, which gives possibility to turn the band structure [14]. In this work, the representative material among TMDs, MoS_2 was studied, due to its high activity, stability, low cost, and tunability. Compared to noble metal catalysts, MoS_2 is relatively inexpensive and abundant. At the same time, its good electrical conductivity, large surface area and good adsorption properties for CO_2 make it a promising candidate for practical applications.

1.2. Research Objectives

Catalytic performances of MoS_2 are studied in this thesis, as it is a representative material of TMDs. MoS_2 has a layered structure of hexagons that consist of covalently bonded Mo and S atoms. Monolayer MoS_2 takes a trigonal prismatic coordination phase. Mo atoms plane sandwiched between two S planes. Van deer Waals forces make multiple layers bound together into bulk MoS_2 [15]. The unique structure makes intercalation possible, which may improve its electrochemical performance. Alkali metal and alkali earth metal ions have been shown have the ability to be intercalated in MoS_2 layers [16]. However, the application of calcium ions in this area has not been studied much. In this thesis, surface morphology, surface chemical component, structure changes, and electrochemical performance of Ca^{2+} intercalated MoS_2 will be investigated.

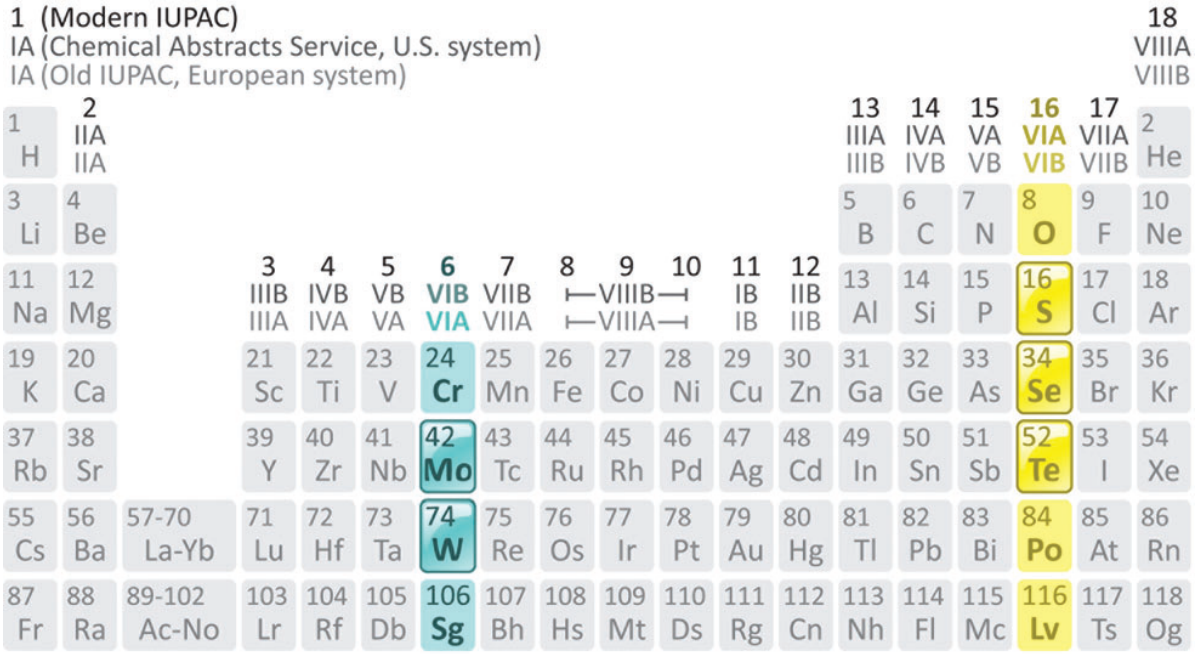

Figure 1.2: Constituent elements of Group 6 Transition Metal Dichalcogenides (TMDs) [13].

1.3. Research questions

This thesis will focus on the following questions:

1. Is it possible to intercalate Ca^{2+} into MoS_2?
2. How the structural and electronic properties of MoS_2 changed after the intercalation?
3. How the catalytic performance of CO_2 reduction changes with the intercalation?
4. What are the products of CO_2 reduction reaction (CO_2RR)?

To answer these questions, several characterization and electrochemical techniques were used in this thesis. In the catalyst preparation stage, dropcasting technique is applied. Ink made of active material (AM), binder and conductivity enhancer used for dropcasting is prepared. Scanning Electron Microscopy (SEM), X-ray Photoelectron Spectroscopy (XPS), X-ray Diffraction (XRD), and Energy Dispersive Spectroscopy (EDS) were used to investigate the morphology, chemical composition, and structural properties of the MoS_2 samples. Three-electrode system electrochemical techniques are used to examine the electrochemical activity. Cyclic Voltammetry (CV) and Electrochemical Impedance Spectroscopy (EIS) were used to test the intercalation potential range, Chronoamperometry (CA) process is used for intercalation. Linear Sweep Voltammetry (LSV) is to access the electrochemical activity. Gas Chromography (GC), High Performance Liquid Chromatography (HPLC) were used to get information about the CO_2RR products.

1.4. Thesis Outline

This thesis consists of 6 Chapters. Chapter 1 gives a brief introduction of CO_2RR and states the research objectives. Chapter 2 covers the literature review of CO_2RR and researched electrochemical

catalysts of CO_2 reduction. Chapter 3 is about the used experimental setups. (The use of experimental instruments, parameter settings, and analysis methods of products will be introduced here.) This is followed by results and discussions in Chapter 4. The conclusion of this thesis and prospective to the future work are shown in chapter 5 and 6, respectively.

2

Literature review

In this chapter, background knowledge and previous studies related to electrocatalytic CO_2 reduction are presented. Section 2.1 provides a thermodynamic perspectives of CO_2 electroreduction. Moreover, challenges faced in CO_2RR are also discussed in this section. Section 2.2 introduces some basic principles and an overview of electrochemical cells. Section 2.3 gives the introduction of performance indicators used in electrocatalytic CO_2RR system. Section 2.5 introduce common materials used in the CO_2RR process.

2.1. Fundamentals of electrocatalytic CO_2RR

Compared with other methods such as photo catalysis and thermocatalysis, the reduction of CO_2 by electrochemical method has the following advantages: (1) The electrode potential can be easily controlled by a potentiostat, and the control of the reaction temperature is relatively simple, which makes the whole reduction process controllable. (2) The electrolytes used in the electrochemical reduction process are readily available aqueous solution with low toxicity. (3) The compact and modular electrochemical systems are relatively easy for scale-up applications [17].

The electrochemical reduction of CO_2 involves many different reaction mechanisms, the intermediate and final products differ depending on the number of protons and electrons involved in the reaction [18]. The activation of the CO_2 molecule to form the radical intermediate (CO_2^-), which is the first step of one electron CO_2RR, is very difficult. As CO_2 is stable, the very negative redox potential (-1.9 V versus SHE in water) makes the electron transfer hard to realize [11]. However, with the help of catalysts, a less negative redox potential is needed for CO_2RR, but the conversion routes are quite different, more electrons are involved in this processing, protons are also involved in the reaction [18]. The final products like formic acid (HCOOH), carbon monoxide (CO), ethylene (C_2H_4), methanol (CH_3OH), ethanol (C_2H_5OH), methane (CH_4), etc. can be used as chemical feedstock [19]. Some products, corresponding CO_2RR half-reactions and potentials are shown in Table 2.1.

pH of the electrolyte also affects the thermodynamics of CO_2RR. As shown in Figure 2.1, at lower pH, CO_2RR is thermodynamically possible when less negative potential is applied. When the pH becomes higher, CO_2RR requires a more negative potential to proceed, which means more energy is consumed [20].

The CO_2RR still faces many difficulties, mainly as follows:

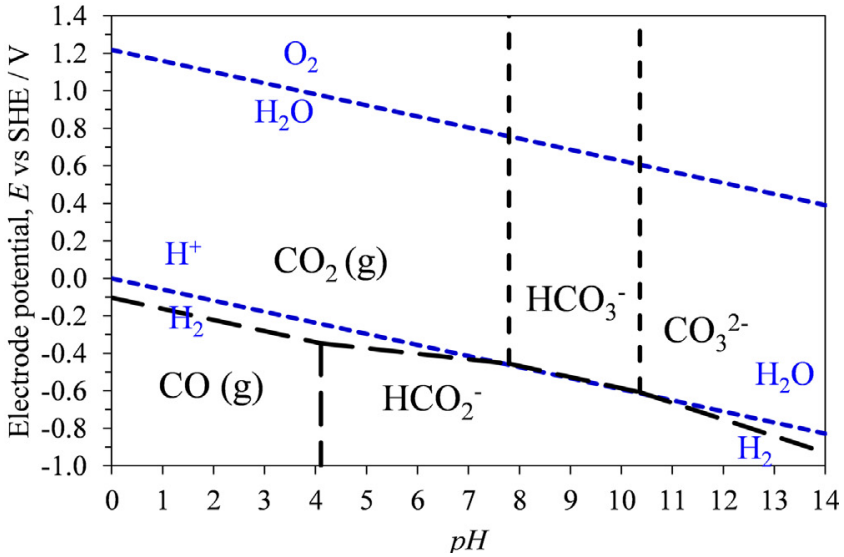

Figure 2.1: Meta-stable potential-pH diagram at 298 K and 10^5Pa [21].

1. The electrochemical reduction of CO_2 in an aqueous electrolyte inevitably produces hydrogen gas. The Hydrogen Evolution Reaction (HER) will compete with CO_2RR, which causes less carbonaceous products [18]. In electrolytes with relatively high pH, the HER reaction is suppressed due to the lack of protons. But in the acidic electrolytes, HER is favorable.

2. The carbon dioxide molecule has a unique linear and centrosymmetric structure, and its carbon-oxygen bond length is only 116.3 pm [22]. Its chemical bond is more stable (bond energy of 805 kJ/mol) than the carbon-oxygen bond in carbon monoxide and carbonyls. Thus breaking this bond requires more energy [19].

3. CO_2RR has slow kinetics, resulting the thermodynamically predicted redox potentials are different from the actual situations. More negative potentials are observed in reality [18].

4. The low solubility (about 0.034 M) of CO_2 in the electrolyte also affects the CO_2RR, the maximum current density is limited [18]. When the alkalinity of the solution increases, bicarbonate and carbonate will form (Equation 2.1), which will reduce the amount of active CO_2 that can participate in the CO_2RR reaction, thus the CO_2RR will be further weakened [20].

$$CO_2(aq) + H_2O \rightleftharpoons H_2CO_3 \rightleftharpoons H^+ + HCO_3{}^{2-} \rightleftharpoons CO_3{}^{2-} + 2H^+ \tag{2.1}$$

2.2. Electrochemical cells for CO_2 reduction reaction

There are three electrodes in an electrochemical cell: working electrode, reference electrode, and counter electrode. The electrochemical reduction process of CO_2 occurs on the cathode in the cell, ususlly the working electrode and the reference electrode together form the cathode compartment, its relating half reaction is shown in Equation 2.2. Differences in electrode materials and applied potentials will affect the types and yields of products. As discussed in section 2.1, HER (Equation 2.3) is a competing reaction of CO_2RR, which will reduce CO_2RR efficiency.

$$xCO_2 + nH^+ + ne^- \longrightarrow product + yH_2O \tag{2.2}$$

Table 2.1: Products, corresponding reactions, and equilibrium Potentials for CO_2RR [23].

Products	**Half-Electrochemical Thermodynamic Reactions**	**V vs. SHE**
C	$CO_2(g) + 4H^+ + 4e^- = C(s) + 2H_2O(l)$	-0.210
C	$CO_2(g) + 2H_2O(l) + 4e^- = C(s) + 4OH^-$	-0.627
HCOOH	$CO_2(g) + 2H^+ + 2e^- = HCOOH(l)$	-0.250
$HCOOH^-$	$CO_2(g) + 2H_2O(l) + 2e^- = HCOO^-(aq) + OH^-$	-1.078
CO	$CO_2(g) + 2H^+ + 2e^- = CO(g) + H_2O(l)$	-0.106
CO	$CO_2(g) + 2H_2O(l) + 2e^- = CO(g) + 2OH^-$	-0.934
HCHO	$CO_2(g) + 4H^+ + 4e^- = HCHO(l) + H_2O(l)$	-0.070
HCHO	$CO_2(g) + 3H_2O(l) + 4e^- = HCHO(l) + 4OH^-$	-0.898
CH_3OH	$CO_2(g) + 6H^+ + 6e^- = CH_3OH(l) + H_2O(l)$	0.016
CH_3OH	$CO_2(g) + 5H_2O(l) + 6e^- = CH_3OH(l) + 6OH^-$	-0.812
CH_4	$CO_2(g) + 8H^+ + 8e^- = CH_4(g) + 2H_2O(l)$	0.169
CH_4	$CO_2(g) + 6H_2O(l) + 8e^- = CH_4(g) + 8OH^-$	-0.659
oxalic acid	$2CO_2 + 2H^+ + 2e^- = (COOH)_2(aq)$	-0.500
oxalate	$2CO_2(g) + 2e^- = {C_2O_4}^{2-}(aq)$	-0.590
ethylene	$2CO_2(g) + 12H^+ + 12e^- = CH_2CH_2(g) + 4H_2O(l)$	0.064
ethylene	$2CO_2(g) + 8H_2O(l) + 12e^- = CH_2CH_2(g) + 12OH^-$	-0.764
ethanol	$2CO_2(g) + 12H^+ + 12e^- = CH_3CH_2OH(l) + 3H_2O(l)$	0.084
ethanol	$2CO_2(g) + 9H_2O + 12e^- = CH_3CH_2OH(l) + 12OH^-$	-0.744

$$2H^+ + 2e^- \longrightarrow H_2 \tag{2.3}$$

$$2H_2O \longrightarrow O_2 + 4H^+ + 4e^- \tag{2.4}$$

The counter electrode is anode compartment of a electrochemical cell. The anodic half reaction is shown in Equation 2.4, which is known as oxygen evolution reaction (OER). Both anodic and cathodic processes have contribution to the total cell voltage (Equation 2.5).

$$E_{\text{cell}} = E_{\text{anode}} - E_{\text{cathode}} \tag{2.5}$$

2.2.1. H-type 3 electrode cells

There are three electrodes in a H-type cell: working electrode, reference electrode, and counter electrode. The working electrode and the reference electrode together form the cathode compartment [24]. The material of the working electrode largely determines the efficiency of CO_2RR. When the CO_2RR starts, CO_2 from the electrolyte is chemically absorbed to the surface of working electrode, where electron transfer occurs. Intermediates will form as chemical bond of CO_2 cleaved. After a series of arrangements, intermediates change into the final products, which will be desorbed from the surface to electrolyte. Commonly used reference electrodes are Standard Hydrogen Electrode (SHE), silver chloride electrode (Ag/AgCl) and saturated calomel electrode (SCE). Counter electrode is where anodic reaction (OER) takes place. A Platinum electrode is usually used as counter electrode [25]. The cathode chamber and anodic chamber are separated by a membrane to prevent oxidation of final products. H-type cells are easy to assemble and is widely used in laboratories [24]. A schematic illustration is shown in Figure 2.2.

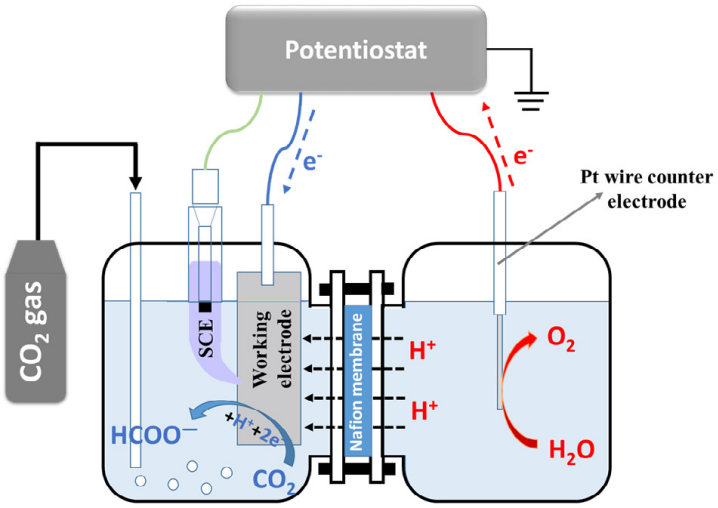

Figure 2.2: H-type cell for CO_2RR [25].

2.2.2. Flow cells

The flow cell, has three electrodes, in which the working electrode and the counter electrode are placed in parallel at a distance, and are separated by the membrane. A micro reference electrode is placed near the working electrode to form cathode compartment. Shortening the distance between these two electrodes helps reduce the resistance introduced by the solution. Flow cells have small chamber for electrolyte and large working electrode surface. So that superior proportion of the electrode surface area to the electrolyte volume (S/V) was obtained (more than 0.5). Such a cell structure enables the liquid products of CO_2RR to quickly reach a relatively high concentration, which is convenient for the analysis. Nuclear Magnetic Resonance (NMR) or High Pressure Liquid Chromatography (HPLC) are commonly used equipment for liquid products analyse [26]. As the CO_2RR progresses, a continuous flow of CO_2 is passed through the cell, the gaseous products of the reduction reaction travel with the gas flow, and they can be analyzed by chromatography (GC) later. For the flow cell, one of the difficulties in the operation is to control the flow rate of CO_2 gas. Fast speed will dilute the obtained gas products, so that they cannot be detected by GC. But slow speed will make the solution not saturated with CO_2, resulting in excessive HER reaction, which will reduce the efficiency of CO_2RR. A schematic illustration is shown in Figure 2.3.

2.2.3. Reactions at the interface of electrodes and electrolytes

CO_2 is dissolved in the electrolyte, so CO_2RR occurs at the interface between the working electrode and the electrolyte. It is critical to understand what happens at the interfacial region in detail. When starting a electrochemical reduction experiment of CO_2, the potentiostatic will apply a negative potential to the working electrode. The surface of working electrode is then negatively charged with electrons, which causes molecules and ions in the electrolyte to interact with the electrode surface. This region is called electrical double layer (EDL) (see Figure 2.4) , where oriented dipoles or charged species can be found. The structure of the double layer influences the process rate of CO_2RR. The total charge density of EDL is equal to that of the electrode and has the opposite sign. The area near the interface is divided into five parts, which are shown below [22].

1. The electrode surface.

2. The inner Helmholtz plane (IHP). IHP is just near the electrode surface, which contains CO_2,

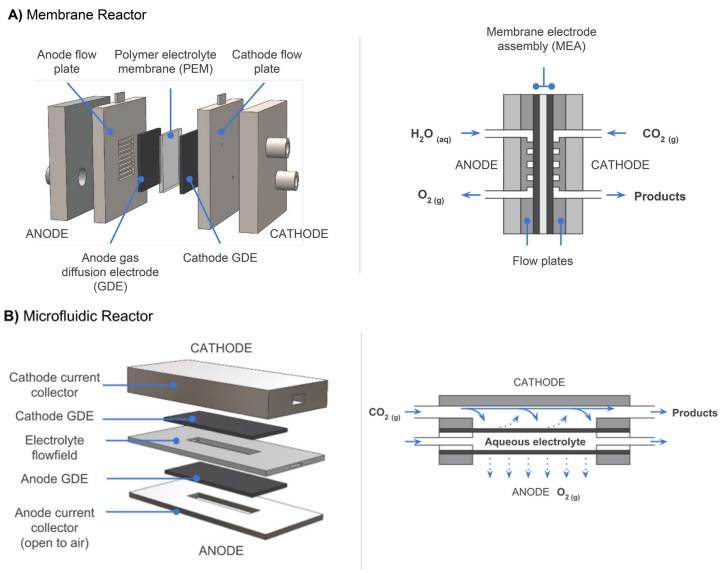

Figure 2.3: Flow cell [27].

CO_2RR intermediates, final products, other solvent molecules, and solvated electrolyte ions.

3. The outer Helmholtz plane (OHP). Some cations in the electrolyte are subjected to long-range electrostatic forces with electrode to form OHP. OHP is affected by the type of cations in the electrolyte.

4. The diffuse layer. Ions in electrolyte that are still affected by the electrode at a further distance are adsorbed to form a diffusion layer, which extends from OHP to the bulk solution.

5. The bulk solution.

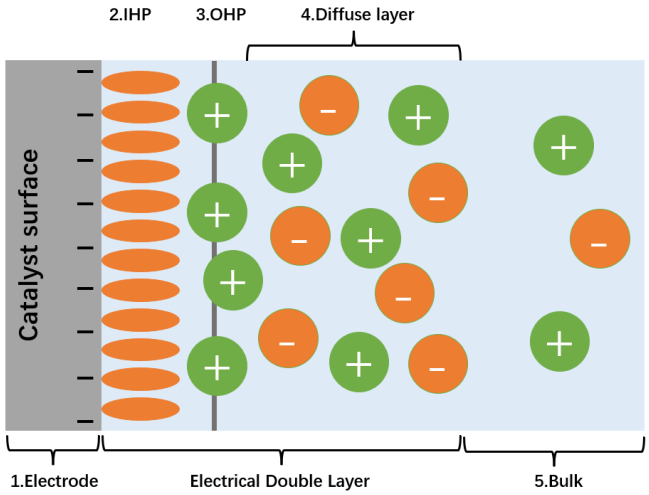

Figure 2.4: The electrical double layer structure at the cathode [22].

Notably, changes in the potential lead to changes in the behavior of the ions in the electrolyte. During the reaction, reactants are consumed and products are formed, which may lead to a concentration gradient. All of these factors contribute to CO_2RR [22].

2.3. Performance indicators for electrocatalytic CO_2 reduction reaction

Some common indicators can be used to compare the CO_2RR systems, and their basic information is introduced in this section.

2.3.1. Faraday efficiency (FE)

Since CO_2RR is not a simple reaction, but multiple reactions are taking place simultaneously at the cathode, the formation of multiple products is inevitable. Some value-added products are expected, while the unwanted HER should be avoided. The generation of undesired products wastes power and causes trouble in separating the products. Therefore, high selectivity is an important factor in evaluating catalytic performance. The selectivity is expressed in terms of Faraday Efficiency, which can be calculated by Equation 2.6, where n is the number of electrons transferred per mole of product, F is the Faraday constant, N is the number of moles of product obtained, and Q is the total charge consumed during the electrocatalytic process [22].

$$FE = \frac{nFN}{Q} \cdot 100\% \tag{2.6}$$

2.3.2. Overpotential (η)

The thermodynamic predictions for the potential of relating half electrode reaction are always less than reality. A much more negative potential is required to get enough disired products. Overpotential (η) is the indicator to represent this extra volatage needed, which was defined as the absolute value of the difference between the applied potential and the thermodynamic predicted potential [22].

$$\eta = \left| E - E^{\mathrm{eq}} \right| \tag{2.7}$$

2.3.3. Current density

Current density is a good indicator to show how fast the reaction taking place, which is defined as the ratio of measured current to working electrode's surface area. Higher current density means higher reaction rate, because the extent of reaction can be reflected by the number of transferred electrons. Using FE of a special product (like CO) multiple overall current density, partial current density (of CO) is got. Partial current density indicates this product's (CO's) generate rate [28].

2.4. Potential versus Standard hydrogen electrode (SHE)

Potential is relative, not absolute. The accurate numbers of applied potentials used in the literature are often potentials versus to the Reversible Hydrogen Electrode (RHE). In the experiment, the reference electrode to be used is generally Ag/AgCl or a Saturated Calomel Electrode (SCE). In order to better compare the results, it is necessary to convert all the used potentials to RHE. Their relationship is as follow:

$$E_{\mathrm{SHE}} = E_{\mathrm{Ag/AgCl}} + {E^0}_{\mathrm{Ag/AgCl}} \tag{2.8}$$

$$E_{\mathrm{SHE}} = E_{\mathrm{SCE}} + {E^0}_{\mathrm{SCE}} \tag{2.9}$$

$$E_{\mathrm{RHE}} = E_{\mathrm{SHE}} + 0.0591 * pH \tag{2.10}$$

Where ${E^0}_{\mathrm{Ag/AgCl}}$ is 0.1976 V at 25°C, ${E^0}_{\mathrm{SCE}}$ is 0.244 V at 25°C, $E_{\mathrm{Ag/AgCl}}$ and E_{SHE} are the applied potentials.

2.5. Common Cathodic Materials for CO_2RR

Commonly used cathodic materials for CO_2RR will be introduced in this section, which are metal catalysts, metal-organic framework (MOFs), doped graphene, and transition metal chalcogenides (TMDs).

2.5.1. Metal catalysts

Using different metals as catalysts for the electrochemical reduction of CO_2 will result in different products. These metals can be divided into four categories according to the reaction mechanism and products, as shown in the Table 2.2.

Table 2.2: Selected metal catalysts for CO_2RR and their reaction products [29].

Group	Electrode	Products
1	Pb, Hg, In, Sn, Cd, Tl	$HCOO^-$
2	Au, Ag, Zn	CO
3	Ni, Fe, Pt, Ti, Ga	H_2
4	Cu	Hydrocarbons

The first group includes Pb, Hg, In, Cd, Sn, and Tl. The CO_2RR product is $HCOO^-$ or HCOOH. Their reaction pathway is ${CO_2}^-$ radical intermediate route (Figure **??** (a)). Using of these metals as catalysts producing little hydrogen, but their electrochemical reduction process requires a high overpotential [30]. Some studies pointed out that Pb and Sn with nanostructure can reduce the overpotential of this process [30]. The second group includes Au, Ag, and Zn. These metals as catalysts can bind with *COOH tightly, so that HCOOH cannot desorb from the electrode. Whether the further reduction reaction can proceed is related to intermediate product can exist stably. *COOH as an intermediate can be further reduced to *CO later, which is weakly bound to these metals. As a result CO is the final produce (Figure **??** (b)). These noble metals have been extensively and intensively studied and are considered to be excellent CO_2RR catalysts due to their high selectivity towards CO. However, these metals are expensive and not widely available materials [31]. The third group is Ni, Fe, Pt, Ti, and Ga. They prefer HER rather than CO_2RR, so the final product will be hydrogen. The last group is Cu. Using Cu as a catalyst can produce a variety of products including HCHO, CH_3OH, and CH_4. Cu can bind *CO tightly, so *CO can be reduced further to $*CH_3$ and other intermidiates (Figure **??**). Under highly alkaline conditions, Cu-based catalysts can also reduce CO_2 to C_2H_4, CH_3CHO, and C_2H_5OH [18]. There are a few ways to increase the selectivity of copper

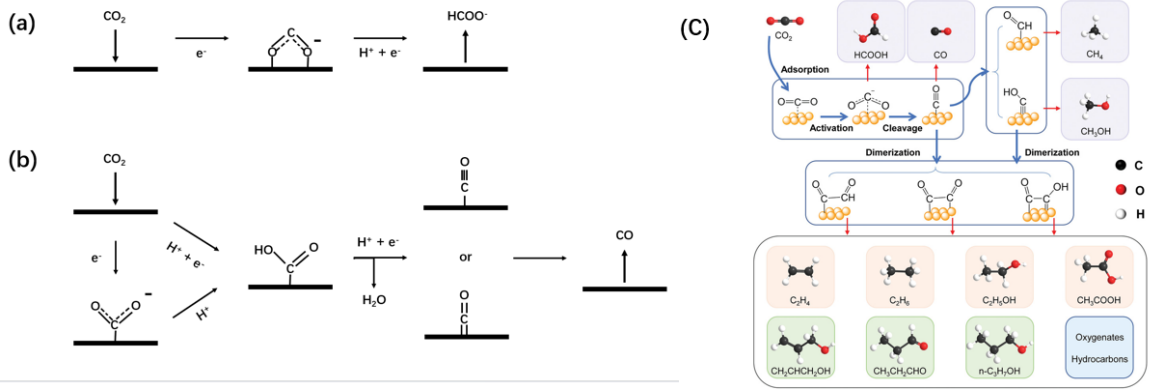

fig:reactionpathway

Figure 2.5: Schematic diagram of the mechanism of CO_2RR (a) on group 1 metal surfaces (CO_2^- radical route). (b) On group 2 surface [30]. (C) On group 4 metal surface

electrodes. For example, using electrolyte with larger cations (Rb^+ Cs^+) instead of electrolyte with smaller cations (Na^+). Large cations can enhance the Faradaic efficiency of the product and in some cases even completely suppress HER [32].

2.5.2. Metal-organic framework

Metal-organic frameworks (MOFs) are porous polymeric materials. Organic ligands as bridges linked metal ions together to form MOFs. When designing MOFs, there are many kinds of metal ions to choose from, and the organic ligands have an infinite variety of possible structures. MOFs can have various optical properties, electronic properties, magnetic properties, and can be used in many applications [33]. Through proper design, MOFs can also be applied in CO_2RR. As CO_2RR catalytic materials, they need high product selectivity, stability, and easily accessible components, all of these can be achieved because of their tunable structure [34]. MOFs inherently have many advantages, such as active sites brought about by a huge surface area, long-range order, and ultra-high porosity [35]. These advantages make MOFs have great research potential. A typical MOF is shown in the Figure 2.6, it is a cobalt-porphyrin MOF, which is highly CO selective (over 76%) and stable (over 7 hours) [34].

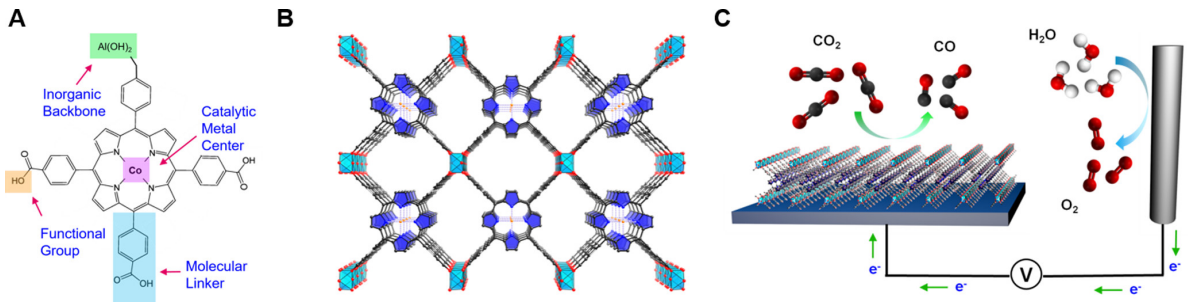

Figure 2.6: (A) A unit of the cobalt-porphyrin MOF. (B) The 3D MOF structure. (C) Use this MOF to achieve a CO_2 electrochemical reduction system [34].

2.5.3. Doped graphene

Compared with precious metal elements, carbon-based materials can be found everywhere. Many carbon materials with unique properties, such as graphene, can be fabricated through clever synthetic methods. The 2D structure, high conductivity, and huge surface area have made graphene attract a lot of attention [36]. Graphene has a large number of catalytic active sites and has been widely used in the field of HER [37]. However, graphene has almost no CO_2 adsorption and activation capabilities, so it is difficult to apply in the field of CO_2RR. Doping can effectively solve this problem. B, N, and Ni as doping atoms can change the structure of graphene, decrease barrier of CO_2 absorption [37]. For example, nitrogen-doped graphene can be used as a catalyst for CO_2RR to produce formate in aqueous solution at room temperature, and the highest FE exceeds 70% [38]. Boron-doped graphene is used as a CO_2RR catalyst, the obtained product is also formate [38].

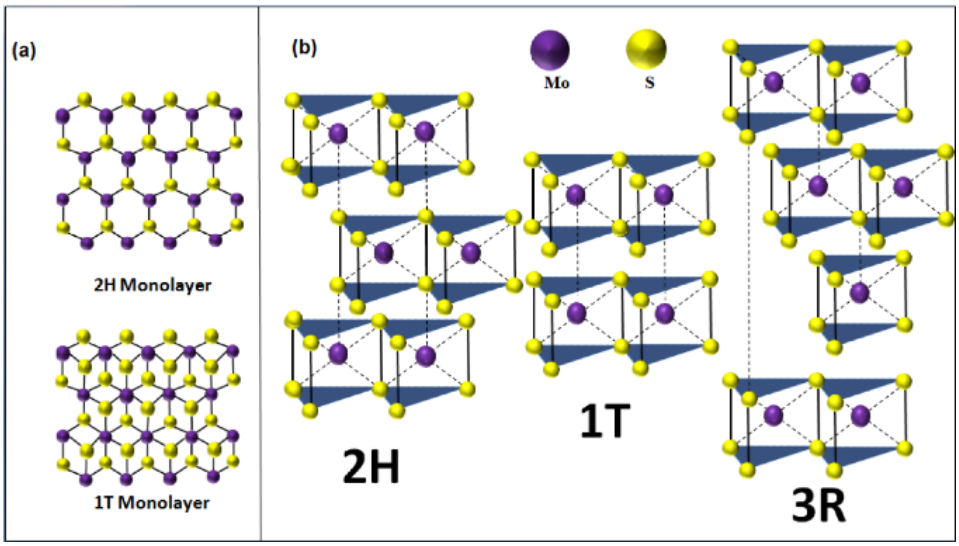

Figure 2.7: (a) MoS_2 monolayer with 2H/1T structure (Top view). (b) Polymorphic structures of 2H, 1T, and 3R MoS_2 [15].

2.5.4. Transition-metal Dichalcogenides (TMDs) catalysts

The chemical formula of transition-metal Dichalcogenides (TMDs) is generally MX_2, where M represents a transition metal such as Molybdenum (Mo) and Tungsten (W), while X represents a chalcogen such as Selenium (Se), Tellurium (Te), and Sulfur (S). TMDs have a typical sandwich structure, a layer of M metal atoms sandwiched between two X Chalcogen layers. Because of this structure, the thickness of TMDs can be only a few atoms (about 0.65 nm) , and their specific surface area is also very large [39, 40]. As a typical representative of TMDs, MoS_2 has three different crystal structures, they are 1T (tetragonal, or octahedral crystal symmetry configuration, meta-stable) , 2H (hexagonal, or trigonal prismatic polytype, most thermodynamically stable phase) , and 3R (rhombohedral, or trigonal prismatic polytype, meta-stable) [15]. Figure 2.7 shows these three structures. MoS_2 with 2H and 3R structure is considered a semiconductor, while MoS_2 with 1T structure is metallic [40]. It is noteworthy that MoS_2 has a direct bandgap (1.88 eV) as a single layer or only a few layers thick [37]. However, the direct bandgap will become the indirect bandgap (1.2 eV) after multiple monolayers form bulk MoS_2 through the van der Waals force [37]. Splendiani et al. found that monolayers MoS_2 have photoluminescence phenomena, which cannot emerge in bulk MoS_2 materials, indicating a bandgap transition [41]. Therefore, the structure has a great influence on the material, and affect their optical and electrical applications. There are several methods which can be used to fabricate 2D MoS_2, the main ones are: mechanical and chemical exfoliations, chemical vapor deposition,

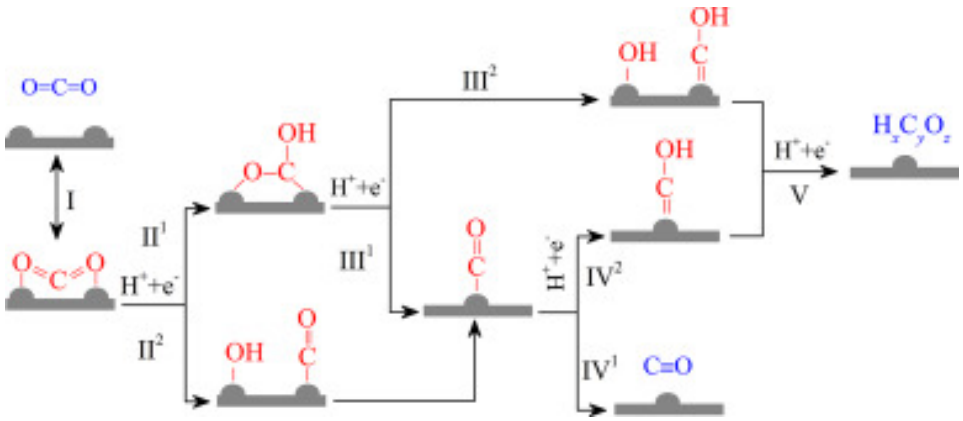

Figure 2.8: Possible reaction pathways for CO_2RR with MoS_2 as catalyst [46].

atomic layer deposition, and pulsed laser deposition [15].

TMDs materials such as MoS_2 have the ability to catalyze HER and CO_2RR [42, 43]. As the most versatile material in TMDs, MoS_2 has a higher reduction current density than noble metal catalysts, which is the reason for choosing it as the CO_2RR catalytic material [44]. When using it as a CO_2 electrochemical reduction catalyst, attention should be paid to slowing down the HER. Improving its stability as a working electrode, increasing the active sites, and achieving relatively high current densities with low overpotentials are also challenges [37]. The active sites with catalytic ability are located on the edges and vacancies, while the pure basal planes are considered have no catalytic ability. The chalcogens (S or Se) located at the edge are well bond with *CHO, *COOH, while *CO are more likely bond with metallic edge sites [45]. Xie et al. [46] used density functional theory (DFT) methods to give the possible reaction mechanism of CO_2RR on MoS_2, which is shown on Figure 2.8. The active sites (grey hills) bind tightly with the intermediates (red molecules), CO and $H_xC_yO_z$ (blue molecules) as final products are desorbed. Abbasi et al found that Metal doping can improve the performance of MoS_2 catalysts. 5% niobium (Nb)-doped MoS_2 has a CO formation turnover frequency (TOF) dozens of times higher than that of the pristine MoS_2. The binding energies of intermediates are modulate during the doping process [47].

2.5.5. Intercalation for MoS_2

Graphite, hexagonal boron nitride (hBN), TMDs, and MXenes have the same characteristics. They are all layered materials, and the layers are connected by weak van der Waals force. These materials have very different electronic, optical and magnetic properties when they are mono-layer and multi-layer [41, 48]. They and also have different catalytic effects when mono-layer materials and multi-layer materials are used as catalysts. Due to the weak van der Waals force between layers, different ions or molecules can be intercalated between layers without destroying the structure of each single layer [49]. This kind of materials is called layered intercalation materials. Lithium ions can be freely inserted and extracted in the gaps of this material, and this discovery has promoted the rapid development of lithium-ion batteries [50].

MoS_2 is thermodynamically stable even in atomically thin form. The narrow interlayer width of MoS_2 limits its further application, intercalation is a potential way so solve this problem [51]. MoS_2 has a layered structure that can hold lithium ions, sodium ions, and other ions into their van der Waals gaps, several methods can make intercalation possible to change the MoS_2 structure [51].

1. Simply immersing MoS_2 to solutions containing the corresponding metal ions (K^+, Na^+, Li^+, Mg^{2+})

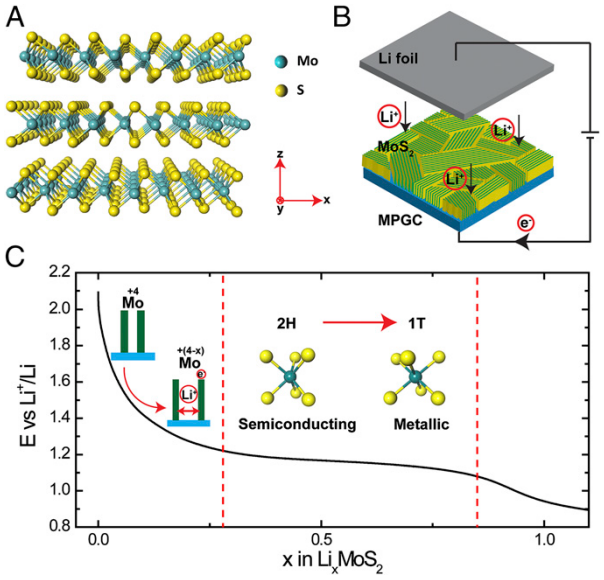

Figure 2.9: (A) MoS_2 with 2H structure. (B) Schematic diagram of the process of intercalating lithium ions into MoS_2 (C) The structure change of MoS_2. With the increase of intercalated lithium ions, MoS_2 changes from 2H structure to 1T structure [16].

[52]. This method is called wet chemical intercalation. It is to immerse the material directly into the solution.

2. Electrochemical charge/discharge processes. Li et al. used THF solution of $Mg(AlCl_3Bu)_2$ (Bu refers to butyl) as the electrolyte, Mg as the anode, and MoS_2 as the cathode to do Mg^{2+} intercalation to MoS_2 [53]. Electrochemical intercalation applies an additional external potential, making intercalation reactions that would otherwise be difficult to occur spontaneously possible.

3. Adding solution containing the corresponding metal ions (Na^+, Ca^{2+}, Ni^{2+}, Co^{2+}) to the solution containing 2 mg/mL 1T-MoS_2 NS. Centrifuging and precipitating the mixed solution, and then washing the precipitate three times with deionized (DI) water [54].

Tunable structure gives possibility to tuning the band structure, charge density, and oxidation state. Wang et al. [16] used a galvanostatic discharge process to control the Li^+ intercalation, and Li_xMoS_2 is formed. They found that layer spacing of MoS_2 can be expanded by Li^+ ions intercalation. MoS_2 will translate from 2H semiconducting phase with trigonal prismatic atomic structure to 1T metallic phase with octahedral atomic structure as intercalated Li^+ ions increased (x increased) , see Figure 2.9. This is because Li^+ donates excessive electrons, these electrons completely change the properties of MoS_2. The Li^+ intercalated MoS_2 showed better catalytic ability for HER [16]. The mechanism of different ions intercalating into the gap of MoS_2 layer is not the same. The intercalation of these ions will also have different effects on the properties of MoS_2. Zou et al. [52] investgated behaviours of Na^+ ions and Li^+ ions intercalated MoS_2. They found that Li^+ is intercalated atom-by-atom, no stable intermediate Li_xMoS_2 formed, while Na^+ is intercalated layer-by-layer, stable intermediates Na_xMoS_2 are formed [52].

The optical properties of MoS_2 also change upon intercalation. Yichao et al. found that the photoluminescence will change after the K^+, Na^+, Li^+ intercalation [16]. MoS_2 with 2H structure has semiconductor properties, so it has photoluminescence phenomenon. After intercalation of ions, the 2H structure transforms into a 1T structure, which has metallic properties and no longer ex-

hibits photoluminescence. This transition is reversible, and the photoluminescence phenomenon is restored after the intercalated ions are extracted.

Various experimental results show that intercalated MoS_2 showed high efficiency to HER and CO_2RR [16, 54]. This shows that its catalytic performance can be improved through intercalation. Because intercalation can increase the carrier concentration, thus increase the conductivity of the material. Thus, this gives a new path for research.

3

Experimental methods

This chapter gives a detailed introduction to the methods used during the experimental work, including characterisation techniques, working electrode preparation, and experimental setup. The general procedures of experiments and the parameters are also listed in this chapter.

3.1. Preparation of working electrode

Glassy carbon is an electrically conductive, electrochemically sable, and gas-impermeable material, thus it is a suitable substrate for electrochemical measurement use in this work [55]. The working electrodes are prepared by drop-casting MoS_2 ink on the top of glassy carbon substrate (Hochtemperatur-Werkstoffe GmbH). It is a simple and widely applicable method. A working electrode with a large surface area and multiple active sites can be easily obtained by using a pipette without the need for other instruments. This method has some disadvantages. Since the micropipette is used manually, the thickness distribution of the film is difficult to control, and the properties of the samples obtained after each drop casting may be different. The drying process may also influence. Trying to control each operation process and drying process to be the same, and control the evaporation rate to obtain working electrodes with similar quality is important. Detailed steps are shown below.

3.1.1. Clean the glassy carbon substrates

Before drop-casting, the glassy carbon substrates are cleaned. First take a glassy carbon substrate, clean it with deionized (DI) water, and then dry it with a cloth. Put the substrate into a test tube, and then add some DI water in it. Sonicate the tube for about 5 minutes. Clean the electrode with DI water and a cloth again. Put the substrate into a test tube with Isopropanol (IPA) in it. Sonicate the tube for about 5 minutes. Finally, take the substrate out and use compressed air to dry it.

3.1.2. Preparation of the ink

The active material (AM), the binder and the conductivity enhancer are the three components of the ink. In this work, the AM is MoS_2, the binder is polyvinyl alcohol (PVA) and the conductivity enhancer is carbon black (CB). The formula is following: 5 wt% PVA + 90 wt% AM + 5 wt% CB. 5 wt% PVA slurry is used to prepare the ink, all the other materials are 99.999% pure.

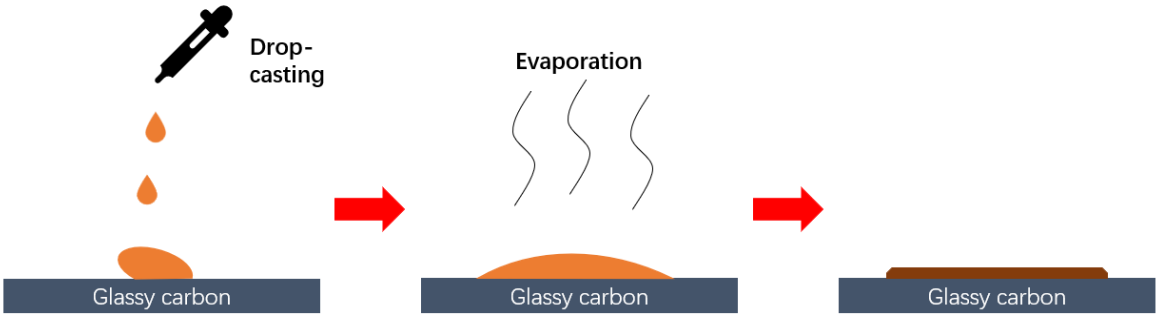

Figure 3.1: Schematic illustration of the drop-casting technique. First unseal the vial of the sonicated ink. And take the micropipette and set it for 20 μL. Then dropcast the ink with the micropipette on the cleaned glassy carbon substrate. Lastly, Let the ink dry. The working electrode is prepared.

First sonicate the 5 wt% PVA slurry for 40 minutes. Then add two drops (about 50 mg) of sonicated PVA slurry into a vial. Calculate the amount of MoS_2 and CB based on the weight of PVA. Add MoS_2 and CB into the vial. Add 2 mL of DI water. Finally, sonicate the PVA-CB-MoS_2 slurry for about 30 minutes. Then the ink is prepared to be dropcasting.

3.1.3. Dropcast the ink

Use micropipette to take about 20 μL ink, drop cast the ink on the cleaned glassy carbon. Leave the ink for several hours until it's completely dry.

3.2. Electrochemical Measurements

Electrochemical measurements help to have a deeper understanding of catalytic activities of samples. Cyclic voltammetry (CV), chronoamperometry (CA), and electrochemical impedance spectroscopy (EIS) were performed, their principle are shown below. Initially, electrochemical experiments were performed in a beaker. The setup of the simple three electrodes system is shown in Appendix (Figure 7.1). Some subsequent experiments were carried out in a electrochemical cell, which is shown in Figure 3.7.

3.2.1. Intercalation process

As mentioned in section 2.5.5, there are many ways to achieve intercalation. In this work, the intercalation process is achieved by the CA process. This electrochemical charge process helps Ca^{2+} ions intercalate to the interlayers of MoS_2. Before and after the CA process, two EIS measurements were used to check whether the intercalation is successful. The specific operation method will be described in detail later.

3.2.2. Cyclic Voltammetry (CV)

Cyclic Voltammetry is a commonly used technique to study oxidation and reduction process of materials. The strength of CV is to study electron transfer-initiated chemical reactions [56]. When

starting a CV experiment, the potentiostat will apply a potential to the cell, which will be recorded as x-axis in voltammograms. As a response, resulting current will be recorded as y-axis in voltammograms. The applied potential varies with time. An important parameter called scan rate (υ) describes this potential variation. Usually, the scan potential starts from a relatively high potential to a set switching potential with the given scan rate, a cathodic trace is gotten. And then return to the initial potential to get the anodic trace [57].

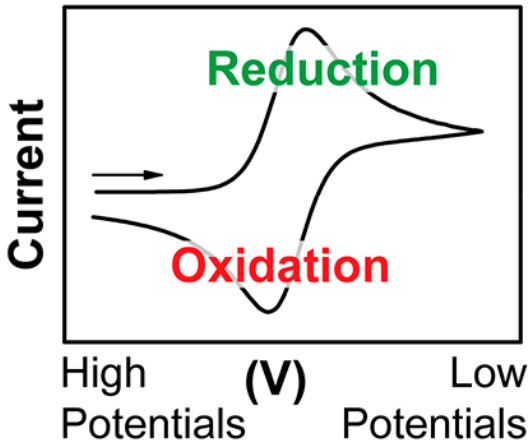

Figure 3.2: A cyclic voltammogram [57]. Scanning starts from a high potential and stops at the switching potential, forming a cathode trace. And then, the scan direction will reverse. A anodic trace will form.

The CV experiments are under the control of a VSP-300 (Biologic) potentiastat. The drop-casted glassy carbon working electrode, which mentioned in Section 3.1, was taped by copper tape and then wrapped with insulating green tape. The green tape is pre-punched with a round hole with a radius of 2 mm, which will be the exposed catalysts area to the electrolyte. The copper tape is for the convenience of connection with the potentiostat. The reference electrode used is a SCE and the counter electrode used is a Pt electrode. CV experiments were performed at the scan rate of 5 mV s^{-1}.

3.2.3. Linear Sweep Voltammetry (LSV)

Linear Sweep Voltammetry (LSV) is equivalent to a one-segment CV test, it sweeps the potential in one direction. During the LSV measurement procedure, a changing potential is given to the working electrode. The potential is changing linearly with time between two set values. Then the current response will be recorded. The output is called a voltammogram, which is current vs. potential. During this project, all LSV experiments were performed using a VSP-300 (Biologic) potentiostat at a scan rate of 10 mV/s.

3.2.4. Chronoamperometry (CA)

Chronoamperometry is a well-established time-dependent technique. During the CA measurement procedure, a static potential is given to the working electrode, the current response versus time is recorded [58]. The catalytic stability of the working electrode can be easily obtained by the CA test. In this work, the intercalation process is realized by CA experiments, which were performed at room temperature with a VSP-300 (Biologic) potentiostat using 1 mM, 5 mM, and 10 mM $CaCl_2$ solution. CA was also performed by GC system in this thesis.

3.2.5. Electrochemical impedance spectroscopy (EIS)

In a three-electrode electrochemical system, for a given current, the voltage loss is due to ohmic or non-ohmic contribution. Ohmic part is well described by resistance, which is time independent. Direct current (DC) techniques is used to study resistance. The non-ohmic part is derived from the adsorption processes, charge, and mass transfer. As the reaction progresses, the substances adsorbed on the electrodes are changing, and the transfer of charge and mass is going on all the time, all of which lead to non-ohmic parts, which is time dependent. The concept of impedance was thus proposed, which is defined as the ratio between the time dependent voltage and the time dependent current. Alternating current (AC) technique is used to study impedance. During a electrochemical impedance spectroscopy measurement, a frequency response analyzer (FRA) is used to create a sinusoidal perturbation. A load bank system will apply this perturbation to the electrochemical system, then the corresponding response signal will recorded by the FRA, and is given in the form of an impedance spectrum. Impedance spectrum come in different forms, mainly used is Nyquist plot and Bode plot [59].

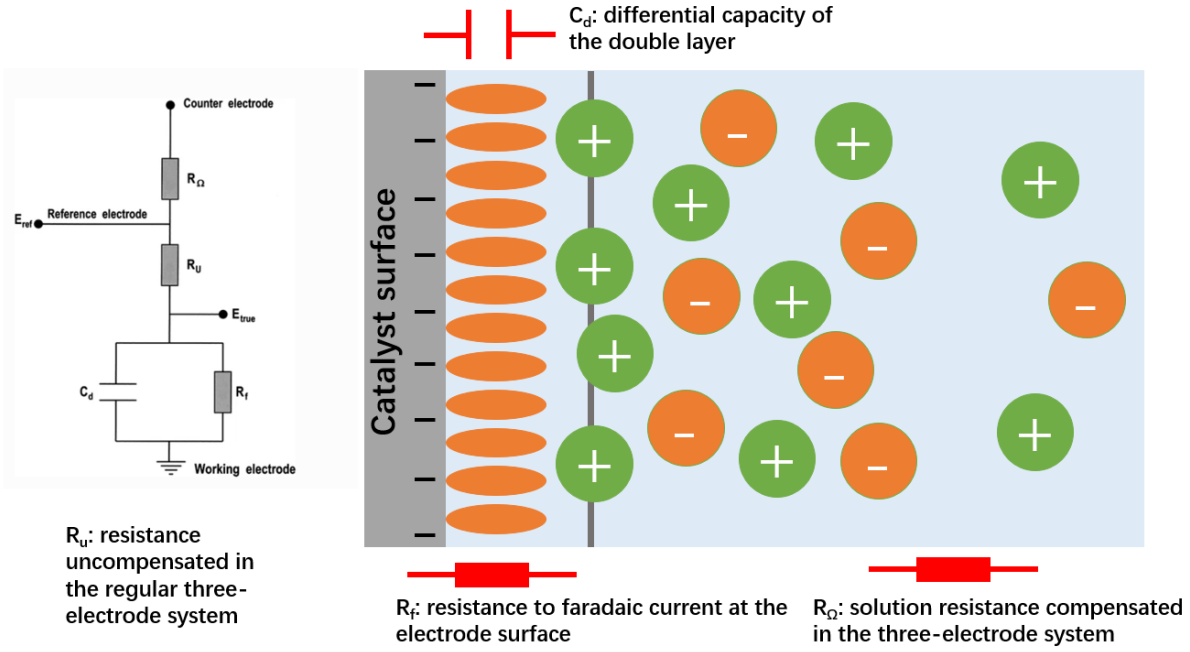

Figure 3.3: (Left) A simple electronic scheme equivalent to the electrochemical cell [60]. (Right) Schemes of redox reaction on the surface.

In electricity, a circuit diagram can visually represent the composition and relationship of each component. The results of EIS can be analysed by fitting and modeling to equivalent electric circuit diagrams [60]. Electronic devices such as resistors, capacitors, and inductors are involved. In a typical electrochemical process, the total impedance includes three parts : the charge transfer resistance R_f, and the electric double layer capacitance C_d, the electrolyte resistance R_Ω, see Figure 3.3. In daaition, extra impedance may caused by diffusion process, which is called Warburg impedance Z_w. If the given frequency of potential perturbation is very large, there is not much mass transformation causing a small Warburg impedance.

In this work, Nyquist plots were chosen for data analysis. The x-axis of the Nyquist Plot is the real part of the impedance and the y-axis is the imaginary part of the impedance. A typical Nyquist Plot is shown in Figure 3.4. The semicircle in the plot is the high frequency region, which is under kinetic control. While mass transfer control the low frequency region. The high frequency region is

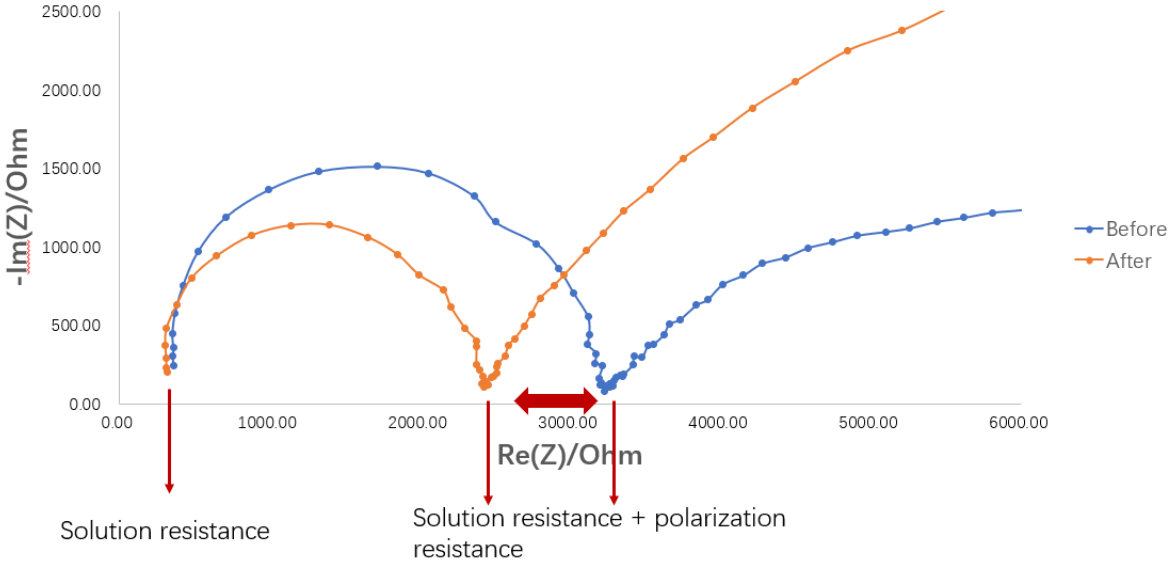

Figure 3.4: Method for analyzing EIS results.

not a full semicircle. Only if the Warburg impedance is equal to zero, the Nyquist plot shows a full semicircle. The nodes on the x-axis of the plot have certain meanings. The left side of the semicircle represents the solution resistance. The diameter of the semicircle represents the Faradic current resistance.

In this work, the EIS experiments were performed by a VSP-300 (Biologic) potentiostat. The frequency range is 1 MHz to 100 mHz. Before and after the intercalation (CA) process, two EIS measurements were used to check whether the intercalation is successful.

Figure 3.4 shows how to analyze whether the intercalation is successful through EIS results. EIS measurement is done before and after CA. If intercalation occurs, the number of charge carriers in the material will increase, and the conductivity will be enhanced, which will be reflected in the EIS figure as a smaller polarization resistance. Comparing the results of the two EIS before and after CA, the smaller the resistance becomes, the more the conductivity of the material increase, thus the number of carriers increases, the more successful the insertion of Ca ions is. Subtraction of $\mathrm{Re(Z)}_{before}$ from $\mathrm{Re(Z)}_{after}$ giver an insight about the conductivity. If the value is negative, the conductivity of the sample is increased. Find at which CA potential the MoS_2 resistance decreases the most. This potential is the optimum intercalation potential.

3.3. Products analysis

The products of CO_2RR will be analysed by gas chromography, whose principle and experiments setup will be introduced in this section.

3.3.1. Gas chromatography (GC)

The volatile products obtained from CO_2 reduction are complex mixtures that may contain various organic compounds. Gas chromatography (GC) can effectively separate these gaseous organic substances and carry out quantitative analysis on them [61]. A simple schematic of GC system is shown in Figure 3.5. Sample injector, column, and detector are the most important components of GC. When performing experiments, gas samples are injected into the GC, and the carrier gas (argon)

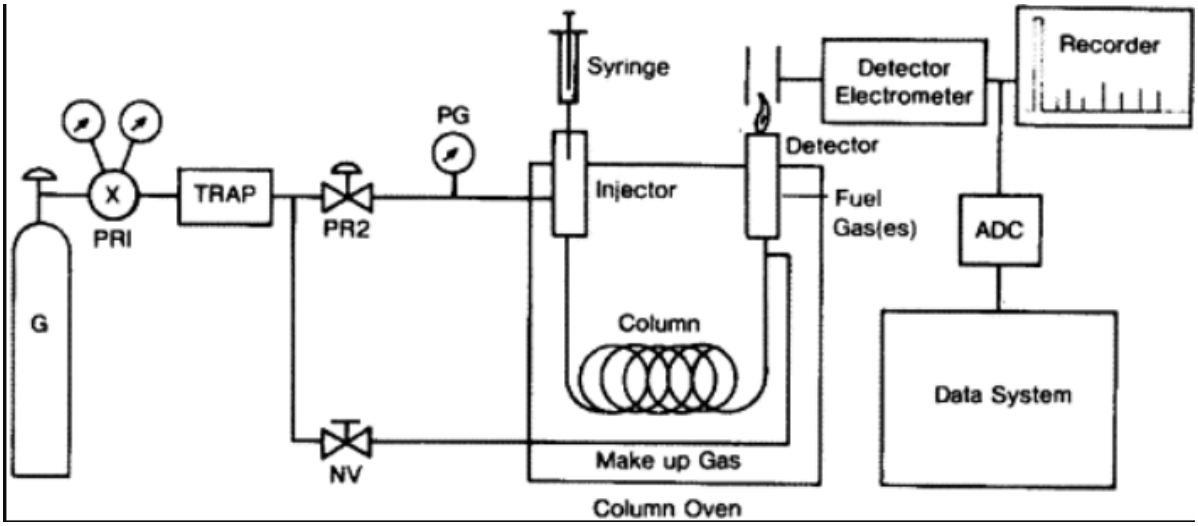

Figure 3.5: Simple schematic of GC system [61].

pushes these samples forward to column. If the samples are not gases, the heating system in the GC will vaporize the samples instantaneously. The column usually uses a metal tube or glass tube with an inner diameter of 1-5 mm and a length of 1-5 m [61]. Long columns will be used to separate samples with more complex compositions, while short columns are suitable for samples with large differences in structure and volatility. The column is coated with a stationary phase (polyethylene glycol or dimethicone). Differences in the reaction of gas phase samples with these stationary phases result in different flow rates of gas phase samples through the column. Then samples are effectively separated. The detector can analyse these separated samples and convert it into electrical signal [62].

In this project, a GC with three chromatographic columns is used, the model is CompactGC4.0 (GAS). Three columns are run simultaneously, connected to different detectors for the detection of different products. Column 1 is connected to a flame ionization detector. Products with different boiling points/vapor pressures will give different signals on this detector, which is mainly used to detect hydrocarbon products. Column 2 and 3 are connected to the thermal conductivity detectors (TCD). The thermal conductivity of the carrier gas is a definite high value, and this detector can determine the types of the gas samples by comparing the thermal conductivity of the gaseous sample and the carrier gas. Column 2 uses He as carrier gas for O_2 and CO measurement, while column 3 uses Ar as carrier gas for H_2 measurement. The electrochemical cell used for CO_2RR measurement is shown in Figure 3.7. The working electrode was glassy carbon coated with (intercalated) MoS_2. An an ion-exchange membrane is used to separate the cathodic and anodic chambers. CO_2 gas flowed into cathodic side of the cell with a rate of 10 mL/min. After reaction with the working electrode, products will flow into GC and be analysed. The electrolyte used was 1.5 mL of 0.1 M $KHCO_3$, which was saturated for 20 mins with CO_2 prior to GC measurements.

3.3.2. High-performance liquid chromatography (HPLC)

The products obtained by the electrochemical reduction of CO_2 include not only gaseous substances such as CO, but also liquid components such as methanol. High-performance liquid chromatography can separate the obtained complex liquid products and quantitatively analyze the content of each component. When starting a test, the degas-unit and pumps will pass the test liquid through a column containing solid adsorbent material. Typically the liquid being tested is called

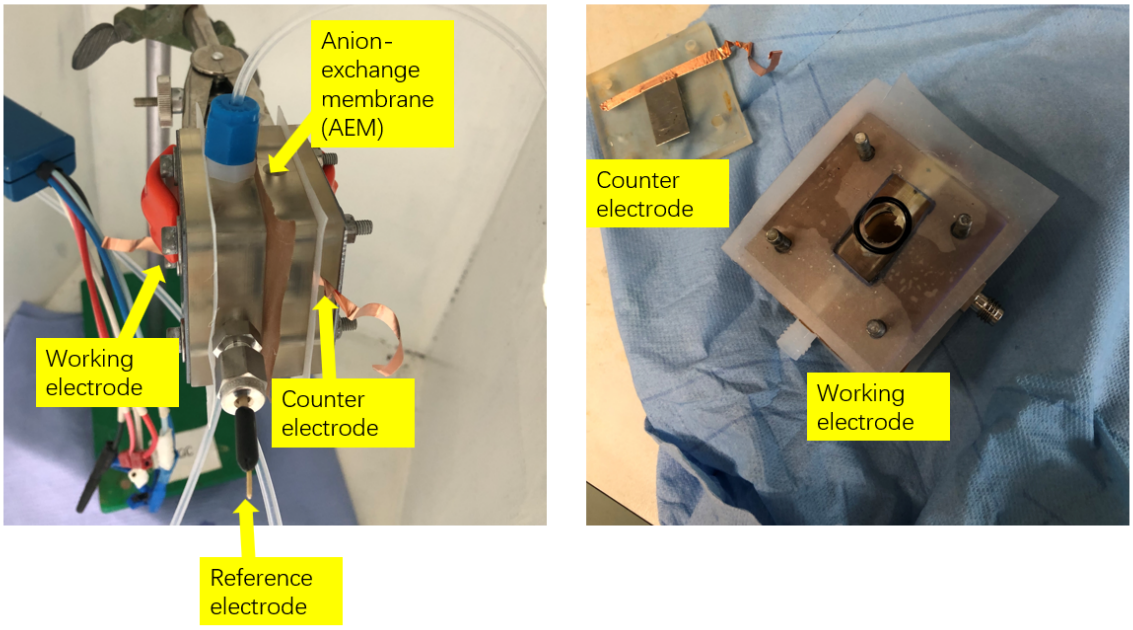

Figure 3.6: Electrochemical cell for CO_2RR measurments.

the "mobile phase" and the column with solid material is called the "stationary phase". Each liquid reacts differently with the stationary phase, causing the different liquids to have different flow rates, so they are separated from each other. In HPLC, the solid particle size in the stationary phase is very small, so it has a strong resolving power. HPLC requires only a small amount of sample to get results [63].

In this work, in order to maximize the product concentration, same electrochemical cell (shown in Figure 3.7) as GC was used. Electrolyte (0.1 M $KHCO_3$) used in the cathodic and anodic chambers was 1.8 mL, separately. After one hour of CO_2 reduction process (CA process), the electrolyte on the working electrode side was retained and tested by HPLC.

3.3.3. Nuclear Magnetic Resonance Spectroscopy (NMR)

HPLC cannot accurately analyze all liquid products in the sample, so Nuclear Magnetic Resonance Spectroscopy is used to further analyze the liquid products. NMR takes advantage of the magnetic properties inherent in some atomic nuclei. These nuclei have a nuclear spin which creates a magnetic moment. When the instrument applies an external magnetic field to the nuclei, the magnetic fields of the nuclei themselves rearrange. At this time, an additional electromagnetic field is applied. When the electromagnetic field has a similar frequency to the nucleus, resonance occurs, and the nuclear spin of the original low-energy level turns to a high-energy level. The radio frequency released when the nuclear spin returns to a low-energy level is the signal received by NMR. By analyzing these signals, the molecular structure can be obtained [64].

In this work, a Bruker Ascend 500 (B0 = 11.7 T) magnet equipped with a NEO console NMR machine was used.

3.4. Surface Characterisation

To study the chemical composition, surface morphology, and structure of the electrocatalyst materials, SEM, EDS, XPS, and XRD were performed. Their basic principles are briefly explained in this part.

3.4.1. Scanning Electron Microscopy (SEM)

Scanning Electron Microscopy (SEM) is a powerful and easy preparation tool to study surface morphology, and crystalline structure of materials. It uses forced electron beams as source to produce image, which gives a higher resolution compared with optical microscopy. That is because electron has shorter wavelength and higher energy than visible light photon (minimum wavelength around 400 nm). Even higher resolution of SEM can be achieved by adjusting the accelerating voltage. When a SEM measurement starts, accelerated electron beams scan over the surface of the specimen. Secondary and backscattered electrons are generated from surface atoms, which will be detected and give morphology about the surface [65]. The disadvantage of SEM is that the penetration ability of electrons is limited, and only the information of the surface part can be obtained.

In this work, a JSM-IT100 SEM with a JEOL-made EDS is used to analyse the surface of the sample. The MoS_2 samples used are conductive, so no additional treatment is required.

3.4.2. Energy-Dispersive X-ray Spectroscopy (EDS)

Energy-Dispersive X-ray Spectroscopy (EDS) is a good tool to qualitatively or semi-quantitatively analyse elemental composition of materials [66]. In an EDS measurement, accelerated electron beams bombard the surface of the specimen. Secondary and backscattered electrons are ejected from surface atoms. But normally, all electrons reside in specific energy levels in an atom, they have positions belong to certain shells, it is what we know as 1s, 1p, etc. When an electron is ejected from an atom, number of electrons reside in this energy level will change, and an positive charged electron hole is leaving. The whole system of the atom becomes unstable. At this time, an electron with higher energy from outer shell is attracted to the hole, energy difference between these energy levels is released as the form of X-ray, which will be detected and give elemental distribution and concentration information around the surface [67].

In this work, a JEOL-made EDS in a JSM-IT100 SEM is used to analyse the surface of the sample.

3.4.3. X-ray Photoelectron Spectroscopy (XPS)

X-ray Photoelectron Spectroscopy is a surface-sensitive analysis technique [59]. It helps to assign the chemical states to the measured atoms. An XPS has several components, including X-ray source, microscope, camera, analyzer, ion gun, and monochromator crystal. X-ray source emits X-rays to irradiate a material, whose atoms will be excited. Electrons from these excited atoms have ability to jump out from the materials' surface. These escaping electrons will be measured by energy then. Put the number of detected electrons per energy interval versus their kinetic energy as a plot, a spectrum is obtained. The same element from any different material will get the same unique spectrum, thus it is easy to identify surface elements. The spectrum from a mixture of elements is the sum of the peaks of the individual constituents. Therefore, the chemical composition of the material surface can be qualitatively analyzed by the position of the peaks on the spectrum. The area of the peak can help quantitatively analyze the corresponding element content. The larger the area, the higher the corresponding element concentration.

3.4.4. X-ray diffraction (XRD)

X-ray diffraction is a nondestructive technique to study chemical composition, crystalline structure, crystallite size, and physical properties of materials. When starting a XRD measurement, a monochromatic beam of X-ray photons will be applied through the sample. By detecting the intensity and direction difference between pristine photons and scattered photons, information about material is gotten. The angle between the diffracted rays can be calculated through some formulas to obtain information such as atomic arrangement and chemical bonds [59].

In this work, Bruker D8 Advance diffractometer Bragg-Brentano geometry and Lynxeye position sensitive detector were used. The radiation is Cu Kα. The measuring angle is 5-110 degrees (step size 0.040 degree) and 5-120 degrees (step size 0.010). Bruker software DiffracSuite.EVA vs 6.0 were used for data evaluation. The interlayer spacing can be obtained from XRD results.

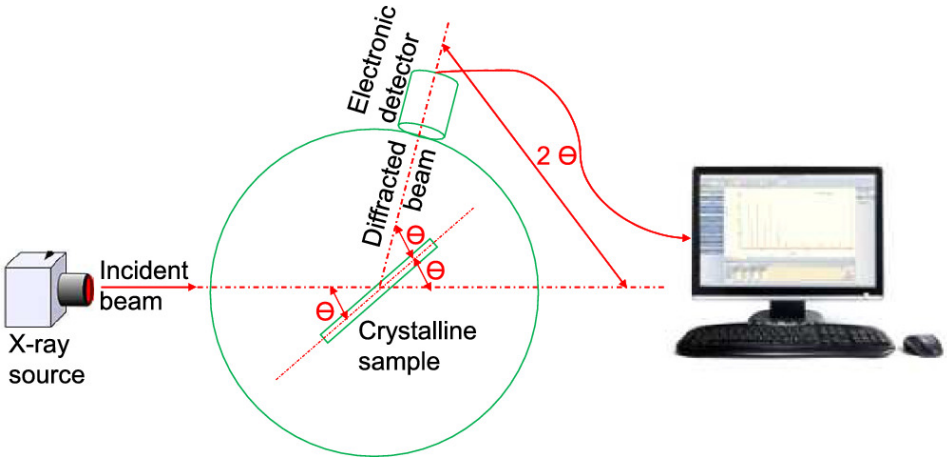

Figure 3.7: XRD instrument schematic [68].

4

Results and discussion

In this section, the experimental results and discussions for CO_2RR experiments using (intercalated) MoS_2 as a catalyst will be presented. MoS_2 catalytic performances in terms of current density and product selectivity are discussed. The catalyst characterization will also be discussed here.

4.1. Electrochemical Measurements

In this section, part of the electrochemical experiments are to realize the intercalation process of Ca^{2+} ions. CA process is used for intercalation, and EIS results can reflect the best intercalation potential. After these tests, LSV was used to test the relevant properties of MoS_2 in the electrochemical CO_2RR.

4.1.1. EIS

As mentioned in section 2.5.5, the charging and discharging process can help ions enter the interlayer of MoS_2. In this work, the method of CA is used to intercalate Ca^{2+} ions. An appropriate potential applied to the working electrode provides the insertion of $Ca_2{}^+$ ions. In the $CaCl_2$ solution at 1 mM, 5 mM, and 10 mM concentrations, the MoS_2 working electrode was applied with different potentials ranged from -2.0 V to -2.5 V vs SCE. It is near the potential where the redox peak appears in the CV test (7.1).

During the intercalation process, charge transfer will occur, resulting in a change in the carrier number, and the electrical conductivity of MoS_2 will change accordingly. The results of EIS can find the best potential of intercalation more accurately. Chapter 3 introduced how to find the optimum intercalation potential, the following analysis are based on the methods described above.

As shown in Figure 4.1 (a), MoS_2 was subjected to the CA process in 1 mM $CaCl_2$ solution at different potentials, and the conductivity changes before and after the CA process were compared. It was found that the conductivity of MoS_2 became higher at the potential of -2.3 V vs SCE. So, this potential is the intercalation potential in 1 mM $CaCl_2$ solution. At this potential, the average resistance of MoS_2 drops by about 600 Ohms. As shown in Figure 4.1 (b), MoS_2 was subjected to the CA process in 5 mM $CaCl_2$ solution at different potentials. It was found that the conductivity of MoS_2 became better at the potential of -2.3 V vs SCE. So, this potential is the intercalation potential in 5 mM $CaCl_2$ solution. At this potential, the average resistance of MoS_2 drops by about 260 Ohms. As

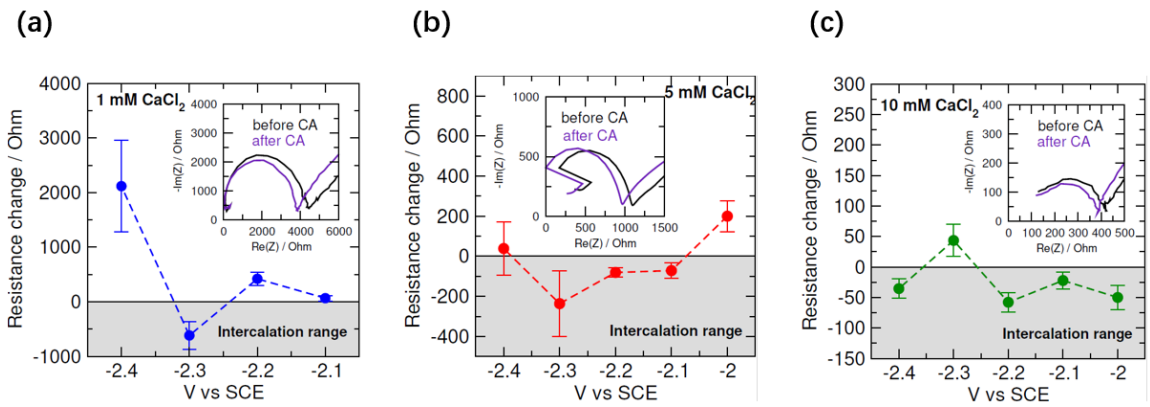

Figure 4.1: (a) EIS results of MoS_2 treated in 1 mM $CaCl_2$ solution. -2.3 V is the Ca^{2+} ion intercalation potential of this concentration. (b) EIS results of MoS_2 treated in 5 mM $CaCl_2$ solution. -2.3 V is the Ca^{2+} ion intercalation potential of this concentration. (c) EIS results of MoS_2 treated in 10 mM $CaCl_2$ solution. -2.2 V is the Ca^{2+} ion intercalation potential of this concentration.

shown in Figure 4.1 (c), MoS_2 was subjected to the CA process in 10 mM $CaCl_2$ solution at different potentials. It was found that the conductivity of MoS_2 became better at the potential of -2.2 V vs SCE. So, this potential is the intercalation potential in 10 mM $CaCl_2$ solution. At this potential, the average resistance of MoS_2 drops by about 60 Ohms. EIS results of other potentials can be found in the Appendix 7.2.

The results of EIS show that the intercalation potential at different concentrations is different. The increase in conductivity is one of the phenomena of intercalation. The results of EIS show that the conductivity has a significant increase at certain potentials, which indicates that Ca^{2+} ions have been intercalated into MoS_2. Observing the EIS results, it can also be found that as the concentration of the $CaCl_2$ solution increases, the potential range in which the intercalation can be successfully performed will become larger, and the intercalation becomes more probable. Therefore, the intercalation process should be done in an electrolyte with a higher concentration. However, oxidation reactions may occur in an electrolyte with high concentration, which is also not suitable for use. The intercalated MoS_2 samples used in subsequent experiments were all processed in 5 mM electrolyte. As the intercalation at this concentration is easy to achieve, and the enhancement of conductivity is significant.

4.1.2. LSV

The electrochemical CO_2 reduction was studied by LSV in 0.1 M $KHCO_3$ as electrolyte, 5 mM $CaCl_2$ solution was used as electrolyte for intercalation process. The green line is the LSV curve (Figure 4.2) of pristine MoS_2 in N_2 saturated solution. Only the reaction of electrolysis of water, that is, HER occurs in the N_2 saturated solution. The red line is the LSV curve of pristine MoS_2 in CO_2 saturated solution. It can be observed that it has higher current density and lower onset potential than in N_2 saturated solution, which means there are other reactions taking place in the CO_2 saturated solution. That is the expected CO_2RR. The black line is the LSV curve of intercalated MoS_2 in N_2 saturated solution. Compared with the pristine sample, it has higher current density, which means the intercalated sample is more conductive. The blue line is the LSV curve of intercalated MoS_2 in CO_2 saturated solution. It has higher current density than that in N_2 saturated solution, which indicates that the sample has a certain catalytic ability for CO_2RR. The current density increases sharply in all cases at around -1.2 V vs SCE. The maximum current density of the pristine MoS_2 sample and

intercalated MoS_2 sample in CO_2 saturated solution reaches -17 mA/cm^2 and -22 mA/cm^2 at -1.7 V vs SCE, respectively. While maximum current density in N_2 saturated solution only shows around -15 mA/cm^2 and -19 mA/cm^2. When comparing the LSV curves of MoS_2 and intercalated MoS_2, it can be found that the latter always has a higher current density, which indicates it has higher conductivity.

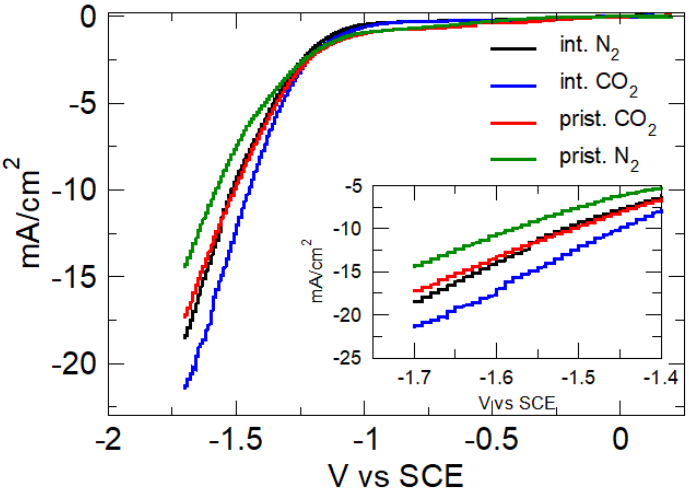

Figure 4.2: The LSV curves of MoS_2 and intercalated MoS_2 samples in CO_2 and N_2 saturated 0.1 M $KHCO_3$ electrolyte.

4.2. Reaction Products of CO_2RR

GC was first used to investigate products of pristine MoS_2 and intercalated MoS_2 in 0.1 M $KHCO_3$ under a potential range from -1.4 V to -1.8 v (vs Ag/AgCl) for 60 minutes. The main products detected for all samples are H_2 and CH_4. After the GC measurement the electrolyte was collected from the cell and analysed by HPLC and NMR. It confirmed the presence of liquid products: formate, ethanol, ethyl acetate, and methanol (Figure 7.7). Furthermore, production of higher hydrocarbons is observed from the FID chromatogram (Figure 7.6).

The average FE of H_2, formate, and methane is calculated and then shown in Figure 4.3. The main procuct is H_2, which indicates HER is dominant. However, a low amount of formate can be found. The main difference of CO_2RR between the pristine and intercalated MoS_2 is observed in the case of methane: there is higher FE for the intercalated MoS_2 than FE of pristine MoS_2.

The adsorbed H_2 on the surface of the working electrode suppress the CO_2RR, thus the FE of CH_4 and other gaseous products of the CO_2RR is low. Using ionic liquids (ILs) as an electrolyte instead of $KHCO_3$ is a potential way to solve this problem. Because ILs have better CO_2 solubility and they can enhance CO_2RR [69]. In ILs, HER can be suppressed.

4.3. Characterization

Characterization results of pristine MoS_2 and intercalated MoS_2 obtained by SEM, EDS, XPS, and XRD are presented and discussed in this section, in order to understand probable changes in the structure of MoS_2 and also the change in surface morphology. Based on previous results, all intercalated MoS_2 samples were obtained by CA in 5 mM $CaCl_2$ solution as electrolyte.

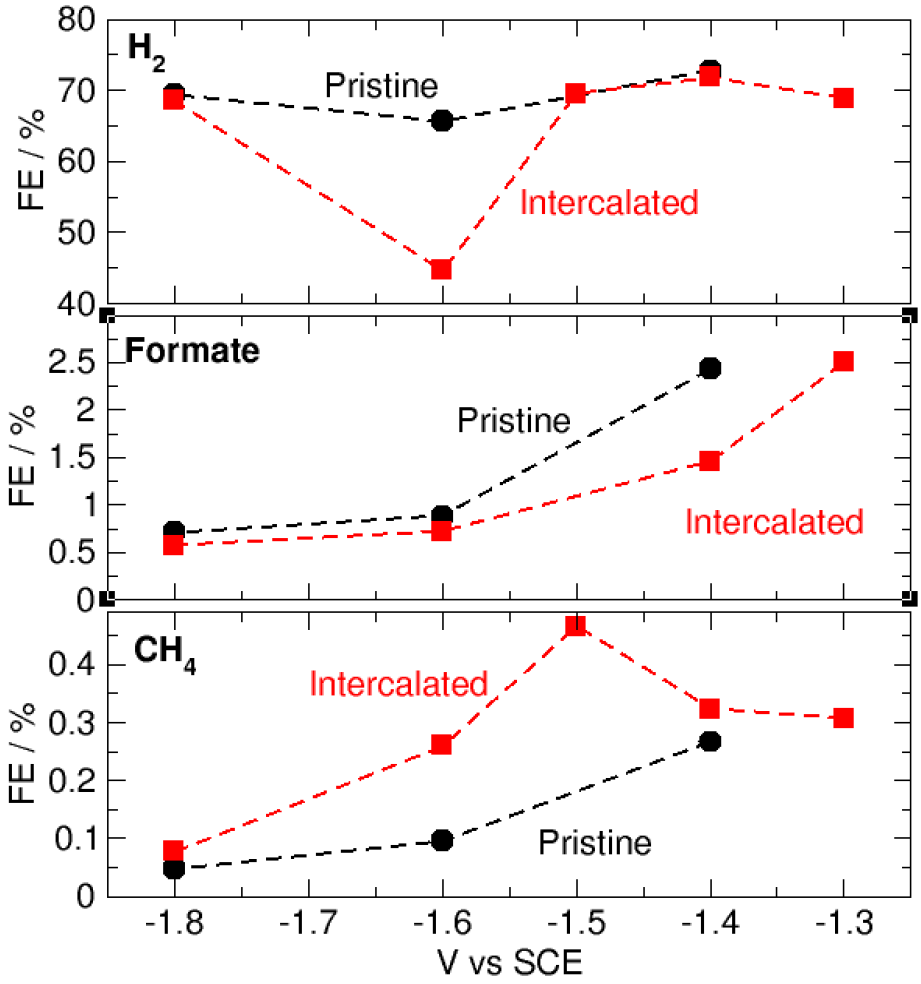

Figure 4.3: The calculated average FEs of H_2, formate, and methane.

Table 4.1: Elemental composition of pristine and intercalated MoS_2 samples from EDS.

	Pristine MoS_2 sample		**Intercalated MoS_2 sample**	
Element	**Mass%**	**Atom%**	**Mass%**	**Atom%**
C	3.24	14.18	15.99	38.71
O	0.26	0.87	12.83	23.31
S	29.29	48.08	24.58	22.29
Mo	67.20	36.87	42.49	13.00
Ca	0	0	3.71	2.69
Total	100	100	100	100

4.3.1. Morphology and sample composition

To better understand the structure and elemental composition of MoS_2 and Ca^{2+} ions intercalated MoS_2, SEM and EDS were performed under 15 kV acceleration potential. It can be seen from Figure 4.4 that the MoS_2 powder is evenly distributed on the glassy carbon substrate. Both pristine and intercalated samples show a highly porous structure. This porous structure brings more active sites and increases the exposure to the electrolyte, thus it is more favorable for catalytic reactions. The similar structure means that the intercalation process did not cause major damage to the sample, and MoS_2 still maintained its basic structure.

Then EDS was used to better understand the elemental composition of the samples. Figure 4.5 (left column) shows the the elemental mapping of pristine MoS_2 sample and Table 4.1 further presents the mass and atomic percentage of each element. It clearly shows that the sample consists of four elements: C, Mo, S, and O. Mo and S signals are from MoS_2 nanopowder. C and O elements are introduced by carbon black and PVA. The oxidation of the sample might occur by air and water contamination.

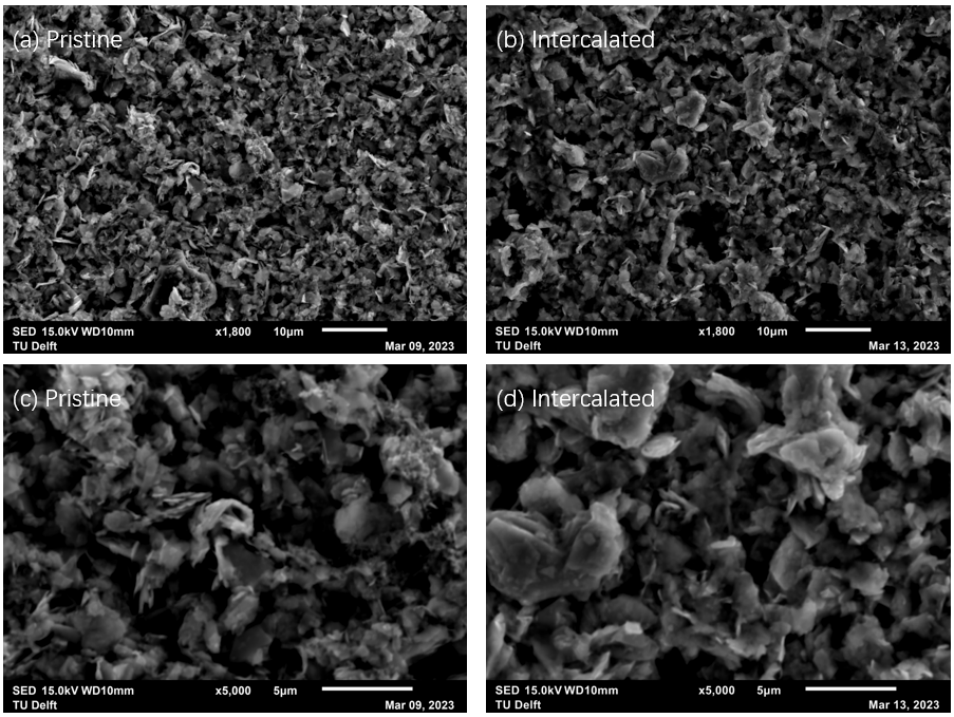

Figure 4.4: (a)(c) SEM image of the pristine MoS_2 sample display its porous structure. (b)(d) SEM image of intercalated MoS_2 sample shows similar porous structure.

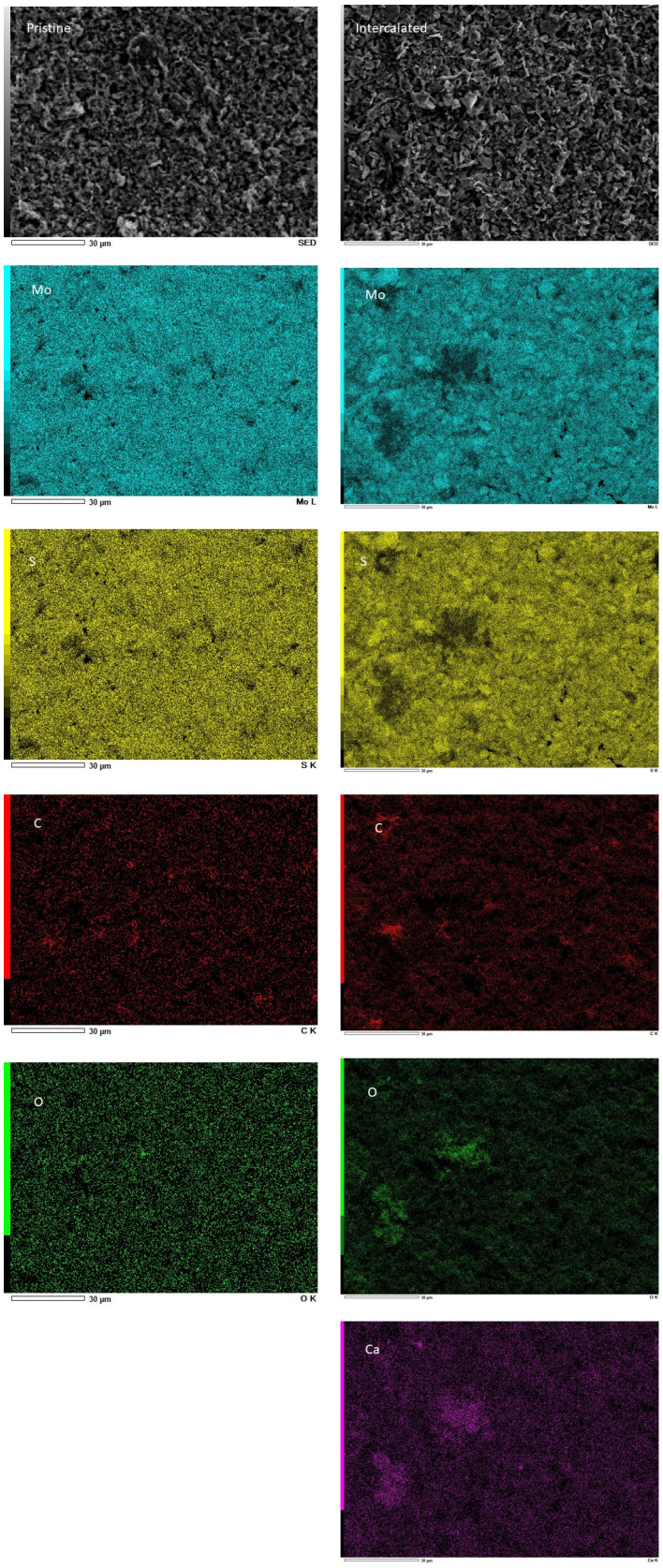

Figure 4.5: EDS elemental mapping of pristine and intercalated MoS_2.

Figure 4.5 (right column) shows the the elemental mapping of Ca^{2+} intercalated MoS_2 sample and Table 4.1 further presents the mass and atomic percentage of each element. It clearly shows that the sample consists of five elements: O, C, Ca, Mo, and S. The EDS mapping confirms the presence of the Ca element in the sample, and the Ca element is distributed uniformly. Oxygen accounts for a relatively large proportion in the sample, which is due to the oxidation in some areas.

4.3.2. XPS

XPS was carried out to analyze the surface chemical composition of the selected samples. Four samples were analysed: pristine MoS_2, MoS_2 treated with 1 mM, 5 mM, and 10 mM $CaCl_2$ solution. Figure 4.6 shows the survey spectra and Table 4.2 shows the atomic% calculated from the survey spectra. It clearly shows that the latter three samples are consist of five elements: C, O, Ca, Mo, and S. There is no Ca element detected from pristine MoS_2 sample.

Table 4.2: Elemental composition of MoS_2 samples treated with $CaCl_2$ with different concentration from XPS survey spectra.

	Atomic%			
Band	**Pristine MoS2**	**1 mM**	**5 mM**	**10 mM**
C 1s	53.1	69.1	69.9	67.9
O 1s	39.1	25.6	24.2	26.3
S 2p	5.8	3.1	3.1	2.7
Mo 3d	2.1	1.4	1.6	1.8
Ca 2p	0	0.8	1.2	1.2

The C 1s spectra (Figure 4.7) of all samples had a strong peak at 284.5 eV, which indicates carbon [70]. This is due to the addition of carbon black and PVA. The PVA added to MoS_2 as a binder contains C-C bonds and C-O bonds (in alcohols). C-O bond (in alcohols) should have a strong peak at 286.5 eV [70]. Carbon in the air may also contaminate the samples.

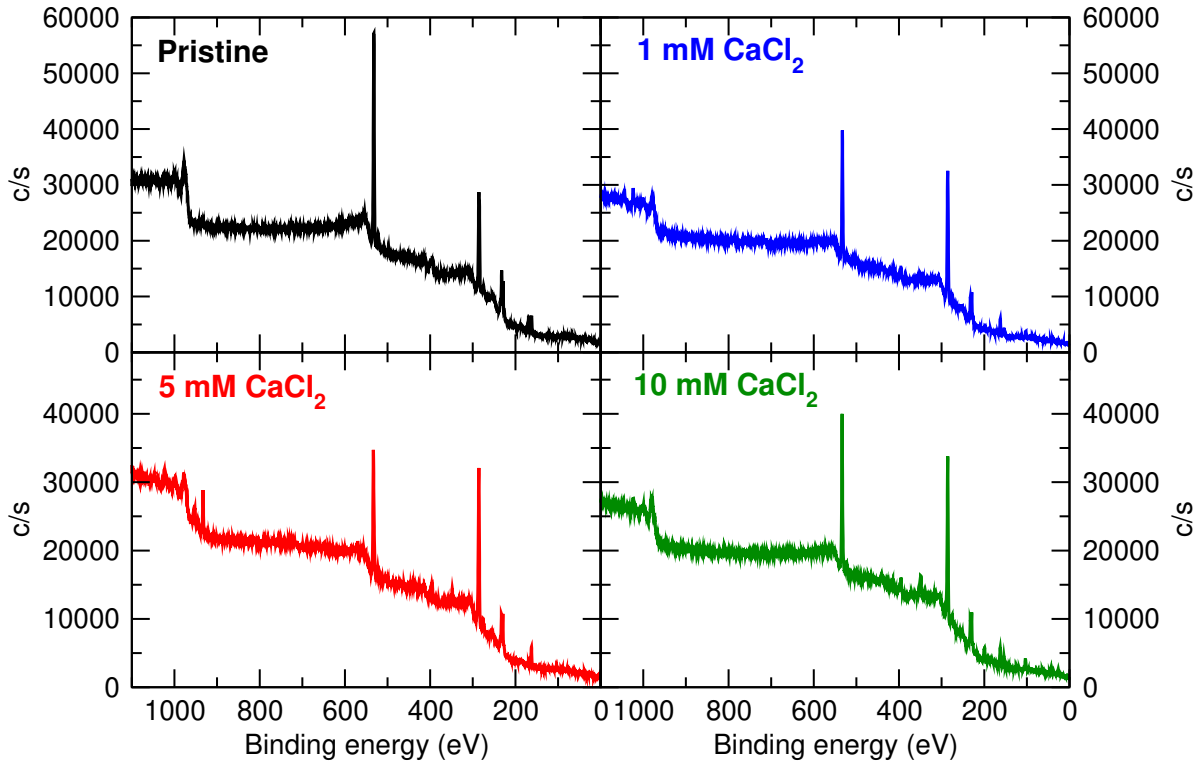

Figure 4.6: XPS spectra of MoS_2 treated with different concentrations of $CaCl_2$ solution.

The peak of the O 1s spectra (Figure 4.7) for pristine MoS_2 is due to pure oxygen (531 eV) mainly [70]. Oxygen in the air caused some contamination to the sample. It can be seen that the O 1s peak of the 5 mM sample has more metal oxides components (528 to 531 eV) [70]. Thus it can be inferred

that metal oxides were formed. Oxygen contamination affect all the samples greatly, the proportion of oxygen is very large.

The Mo 3d5 spectra of pristine MoS_2 (Figure 4.7) show two peaks at around 232.33 and 229.17 eV, which denote Mo 3d3/2 and 3d5/2 with spin-orbit splitting energy of 3.16 eV. The 3d5/2 peak of MoS_2 is near 229 to 230 eV [70], which is consistent with the observed results. The peak at 226 eV shows the S 2s band. A small right shifting of the peaks was observed in the three intercalated samples, the spin-orbit splitting energy are still around 3.16 eV. The shift of the Mo peaks indicate the intercalation of Ca^{2+} ions. This is because when Ca^{2+} is intercalated into interlayers, MoS_2 will transform from a semiconducting 2H structure to a metallic 1T structure. It is reflected in the XPS spectra that the Mo 3d5 peak of MoS_2 with 2H structure has higher binding energy, and the Mo peak of MoS_2 with 1T structure has lower binding energy [71].

The S 2p3 spectrum of pristine MoS_2 (Figure 4.7) show two peaks at 162 and 168.8 eV. The 162 eV peak is also observed in the intercalated samples, which denotes sulfide (160 to 164 eV) [70]. The peak at 168.8 eV shows the presence of S-O band in the case of pristine sample [70]. This peak disappears for the intercalated samples, while more metal oxide appears (O 1s spectra as evidence).

The Ca 2p3 spectra (Figure 4.7) of all intercalated MoS_2 samples have peaks at around 347.5 and 351 eV, which denote Ca 2p3/2 and 2p1/2 with spin-orbit splitting energy of 3.5 eV [70]. No peaks are observed in the pristine sample. It can be observed that the Ca 2p3/2 peak of the sample intercalated in 1 mM $CaCl_2$ solution is located at 348 eV, which is the peak of $CaCl_2$[70]. It is speculated that not many calcium ions were intercalated into the MoS_2, which may be due to the low amount of calcium ions. The peak of Ca 2p3 has an obvious right shift with the increasing of $CaCl_2$ concentration. The Ca 2p3/2 peak of the samples treated in 5 mM and 10 mM $CaCl_2$ solution is around 347 eV, which is near to the peak of CaS [70]. This shift shows the presence of CaS, which means the intercalation is successful.

Figure 4.7 shows the band gap structure of the pristine and intercalated MoS_2. Comparing the band gap structure of the samples, The slope of 5 mM sample has a significant change, which is due to the intercalation.

4.3.3. XRD

X-ray Diffraction was carried out to analyze the chemical components and interplanar spacing of the selected catalysts. Four samples were analysed: pristine MoS_2, MoS_2 treated with 1 mM, 5 mM, and 10 mM $CaCl_2$ solution.

The XRD pattern (Figure 4.8 left) of all samples had strong peaks at around 14.378 2θ assigned to (002) direction of MoS_2 crystal, around 39.539 2θ assigned to (103), around 44.152 2θ assigned to (006), around 49.788 2θ assigned to (105), and around 58.336 2θ assigned to (110) direction of MoS_2 crystal. These peaks are relatively strong and can be clearly identified from the Figure 4.8. This indicates that the main component of the sample is MoS_2, and its crystallinity is good. A broad peak can be seen near 25 2θ, which does not belong to any of the MoS_2 peaks, but to C. This is due to the addition of carbon black to the sample in order to enhance the conductivity.

Figure 4.8 shows MoS_2 (002) peaks of all the samples. Pristine MoS_2 has a peak of 14.4086 2θ, MoS_2 treated in 1 mM $CaCl_2$ solution has a peak of 14.3693 2θ, MoS_2 treated in 5 mM $CaCl_2$ solution has a peak of 14.3861 2Theta, MoS_2 treated in 10mM $CaCl_2$ solution has a peak of 14.4127 2θ. The second and third samples have 2θ reductions of 0.0393 and 0.0225, respectively, compared to the

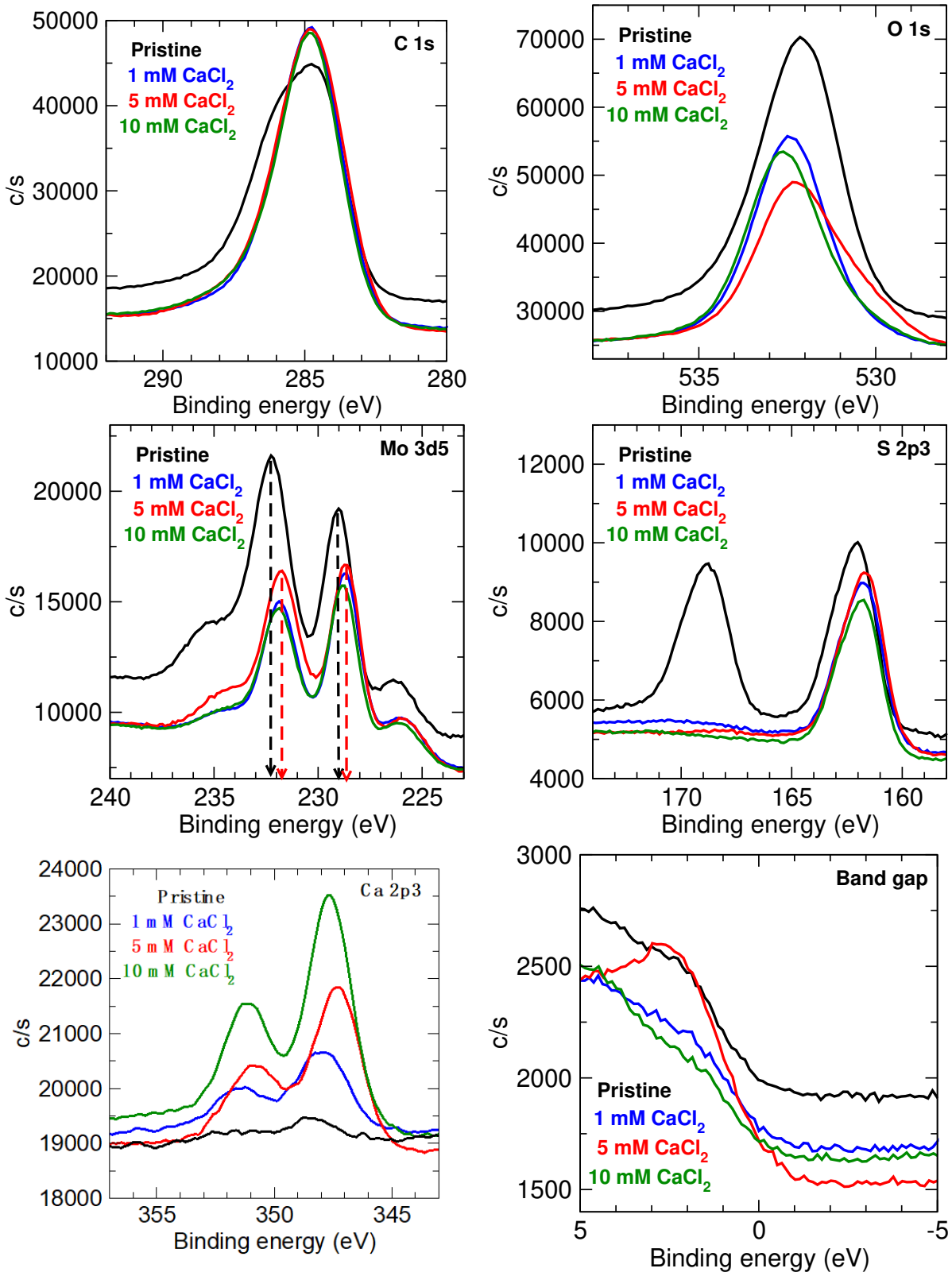

Figure 4.7: High-resolution XPS spectra for different forms of MoS_2 and band gap structure spectra.

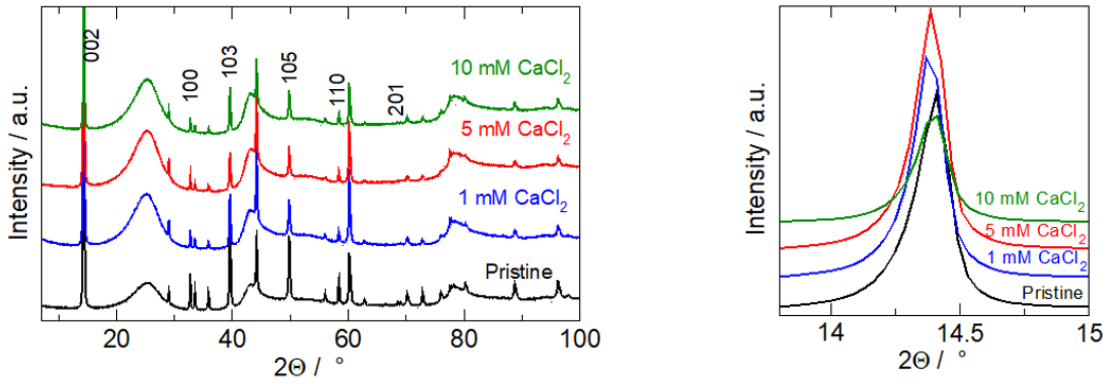

Figure 4.8: XRD pattern for pristine and intercalated MoS_2 samples. XRD pattern between 14 to 15 degrees 2θ is also shown.

Table 4.3: Layer spacing estimated from XRD results.

Sample	Estimated interlayer spacing (nm)
Pristine	0.614235
1 mM	0.615910
5 mM	0.615192
10 mM	0.614064

pristine sample. According to the Bragg equation:

$$n\lambda = 2d * sin\theta, \tag{4.1}$$

where n is the diffraction order (n = 1 here), λ is the X-ray wavelength (Cu kα radiation with λ = 0.15406 nm), d is the spacing of the diffracting planes, and θ is the angle between the incident rays and the diffracting planes.

This means that the interplanar spacing of these two samples in the (002) direction has increased. The increased interlayer spacing brings evidence for the successful intercalation of Ca^{2+} ions in these samples.

The estimated interlayer spacing can be found in Table 4.3. The calculated results are in good agreement with the reported results of 0.615 nm [72]. It can be seen that the interlayer spacing of the 1 mM sample increased by 0.001675 nm (0.27%) compared to the pristine sample. And the interlayer spacing of the 5 mM sample increased by 0.0000957nm (0.0156%) compared to the pristine sample. Increasing the interlayer spacing can reduce the Gibbs free energy of hydrogen adsorption [72]. This is also consistent with the results observed by GC.

5

Conclusions

In summary, the thesis aims to investigate the intercalation process of $Ca_2{}^+$ ions into MoS_2 and the electrocatalytic performance, i.e. activity, selectivity, of the new material for the electrochemical CO_2 reduction reaction. Intercalation is achieved through CA process. Many evidences show that Ca^{2+} ions are successfully intercalated into the interlayer of MoS_2. The main products of CO_2 RR are formate, methane, ethanol, ethyl acetate, methanol, and formic acid.

From the results of EIS, it can be seen that as the concentration of the $CaCl_2$ electrolyte increases, Ca^{2+} ions can be more easily intercalated into the MoS_2 interlayer under a wider range of potential. Intercalated MoS_2 has better electronic properties (higher conductivity).

The LSV results show that the intercalated sample has a higher current density than pristine sample, which means that it has better electronic properties and a higher catalytic activity. Both samples have larger current densities in CO_2-saturated solutions compared with N_2-saturated solution, which indicates that both samples had catalytic activity for CO_2RR.

XPS results show that the band structure of MoS_2 is changed. The pristine MoS_2 has a 2H structure with semiconductor properties, while the structure of intercalated samples is changed towards the 1T structure with metallic properties.

XRD results show that the interlayer spacing in the (002) direction increases, which confirmed the intercalation of $Ca_2{}^+$.

6

Future Outlook

During the experiments, the setup of the electrochemical system, the electrolyte, the solubility of CO_2, and many other factors may be the limitations which need to be further improved. In this section, some recommendations are proposed as reference for future study.

1. There are few studies on potential in this work. The potential range applied in the CO_2RR process has an influence on the results. The FE may change in different potential ranges. Finding the potential range with the maximum FE is a good subject for research.

2. The electrolyte also has a great influence on the results during CO_2RR. The species, concentration, and pH of the electrolyte all have an impact on the type, output, and proportion of the products. It is also a good research direction to study the influence of different types and concentrations of electrolytes on the results. However, it is relatively difficult to control the pH at the reaction interface between the electrode and the electrolyte. ILs have better CO_2 solubility, can suppress HER, and can adjust pH more conveniently, so follow-up studies can use ILs as electrolytes.

3. In this work, the bandgap structure of MoS_2 can be changed by intercalating Ca^{2+} ions, but the result of the change is uncontrollable. The quantity and position of the intercalated Ca^{2+} ions are difficult to control, and sometimes the desired bandgap structure cannot be obtained. More advanced and controllable intercalation methods should be proposed in the future. Or a better method for changing the bandgap structure should be proposed, and a pre-designed bandgap structure can be obtained by this method.

4. Other TMDs such as WS_2 are also capable of electrochemical catalysis. At the same time, other materials with similar structures are also good research objects in the future.

5. The GC results showed, the main product of electrochemical CO_2RR is still H_2. It indicates the HER dominates over the CO_2RR, thus engineering the surface of the catalyst should be useful to promote the CO_2RR. For example. putting a polymer layer on the sample.

Bibliography

[1] C. Beer, M. Reichstein, E. Tomelleri, P. Ciais, M. Jung, N. Carvalhais, C. Rödenbeck, M. A. Arain, D. Baldocchi, G. B. Bonan, et al., *Science* **2010**, *329*, 834–838.

[2] W. meteorological organization, **2021**.

[3] N. N. C. for Environmental Information, **2022**.

[4] J. Tollefson, *Nature* **2020**, *580*, 443–446.

[5] S. A. Kulp, B. H. Strauss, *Nature communications* **2019**, *10*, 1–12.

[6] J. R. Malcolm, C. Liu, R. P. Neilson, L. Hansen, L. Hannah, *Conservation biology* **2006**, *20*, 538–548.

[7] A. Olabi, M. A. Abdelkareem, *Renewable and Sustainable Energy Reviews* **2022**, *158*, 112111.

[8] S. Nyquist, **2016**.

[9] Z. Sun, T. Ma, H. Tao, Q. Fan, B. Han, *Chem* **2017**, *3*, 560–587.

[10] Q. Qin, M. Sun, G. Wu, L. Dai, *Carbon Capture Science Technology* **2022**, *3*, 100043.

[11] Y. Y. Birdja, E. Pérez-Gallent, M. C. Figueiredo, A. J. Göttle, F. Calle-Vallejo, M. Koper, *Nature Energy* **2019**, *4*, 732–745.

[12] E. S. Rubin, H. Mantripragada, A. Marks, P. Versteeg, J. Kitchin, *Progress in energy and combustion science* **2012**, *38*, 630–671.

[13] M. Samadi, N. Sarikhani, M. Zirak, H. Zhang, H.-L. Zhang, A. Z. Moshfegh, *Nanoscale Horizons* **2018**, *3*, 90–204.

[14] M. Chhowalla, H. S. Shin, G. Eda, L.-J. Li, K. P. Loh, H. Zhang, *Nature chemistry* **2013**, *5*, 263–275.

[15] D. Mouloua, A. Kotbi, G. Deokar, K. Kaja, M. El Marssi, M. A. El Khakani, M. Jouiad, *Materials* **2021**, *14*, 3283.

[16] H. Wang, Z. Lu, S. Xu, D. Kong, J. J. Cha, G. Zheng, P.-C. Hsu, K. Yan, D. Bradshaw, F. B. Prinz, et al., *Proceedings of the National Academy of Sciences* **2013**, *110*, 19701–19706.

[17] J. Qiao, Y. Liu, F. Hong, J. Zhang, *Chemical Society Reviews* **2014**, *43*, 631–675.

[18] Z. Sun, T. Ma, H. Tao, Q. Fan, B. Han, *Chem* **2017**, *3*, 560–587.

[19] Y. Zheng, W. Zhang, Y. Li, J. Chen, B. Yu, J. Wang, L. Zhang, J. Zhang, *Nano Energy* **2017**, *40*, 512–539.

[20] M. König, J. Vaes, E. Klemm, D. Pant, *Iscience* **2019**, *19*, 135–160.

[21] P. Bumroongsakulsawat, G. Kelsall, *Electrochimica Acta* **2014**, *141*, 216–225.

[22] X. Zhang, S.-X. Guo, K. A. Gandionco, A. M. Bond, J. Zhang, *Materials Today Advances* **2020**, *7*, 100074.

[23] Y. Cao, Q. Chen, C. Shen, L. He, *Molecules* **2019**, *24*, 2069.

[24] S. Liang, N. Altaf, L. Huang, Y. Gao, Q. Wang, *Journal of CO2 Utilization* **2020**, *35*, 90–105.

[25] C. Zhao, J. Wang, *Chemical Engineering Journal* **2016**, *293*, 161–170.

[26] P. Lobaccaro, M. R. Singh, E. L. Clark, Y. Kwon, A. T. Bell, J. W. Ager, *Physical Chemistry Chemical Physics* **2016**, *18*, 26777–26785.

[27] D. M. Weekes, D. A. Salvatore, A. Reyes, A. Huang, C. P. Berlinguette, *Accounts of chemical research* **2018**, *51*, 910–918.

[28] R. Lin, J. Guo, X. Li, P. Patel, A. Seifitokaldani, *Catalysts* **2020**, *10*, 473.

[29] E. V. Kondratenko, G. Mul, J. Baltrusaitis, G. O. Larrazábal, J. Pérez-Ramırez, *Energy & environmental science* **2013**, *6*, 3112–3135.

[30] R. Kortlever, J. Shen, K. J. P. Schouten, F. Calle-Vallejo, M. T. Koper, *The journal of physical chemistry letters* **2015**, *6*, 4073–4082.

[31] D. L. T. Nguyen, Y. Kim, Y. J. Hwang, D. H. Won, *Carbon Energy* **2020**, *2*, 72–98.

[32] M. R. Thorson, K. I. Siil, P. J. Kenis, *Journal of the Electrochemical Society* **2012**, *160*, F69.

[33] S. L. James, *Chemical Society Reviews* **2003**, *32*, 276–288.

[34] N. Kornienko, Y. Zhao, C. S. Kley, C. Zhu, D. Kim, S. Lin, C. J. Chang, O. M. Yaghi, P. Yang, *Journal of the American Chemical Society* **2015**, *137*, 14129–14135.

[35] D. D. Medina, A. Mähringer, T. Bein, *Israel Journal of Chemistry* **2018**, *58*, 1089–1101.

[36] A. K. Geim, K. S. Novoselov in *Nanoscience and technology: a collection of reviews from nature journals*, World Scientific, **2010**, pp. 11–19.

[37] M. A. Tekalgne, H. Do, A. Hasani, Q. Van Le, H. Jang, S. Ahn, S. Kim, *Materials Today Advances* **2020**, *5*, 100038.

[38] X. Duan, J. Xu, Z. Wei, J. Ma, S. Guo, S. Wang, H. Liu, S. Dou, *Advanced Materials* **2017**, *29*, 1701784.

[39] L. Ma, Y. Li, Y. Xu, J. Sun, J. Liu, T. Wu, X. Ding, Y. Niu, *Electrochemistry Communications* **2021**, *125*, 107002.

[40] X. Li, H. Zhu, *Journal of Materiomics* **2015**, *1*, 33–44.

[41] A. Splendiani, L. Sun, Y. Zhang, T. Li, J. Kim, C.-Y. Chim, G. Galli, F. Wang, *Nano letters* **2010**, *10*, 1271–1275.

[42] M. Zeng, Y. Li, *Journal of Materials Chemistry A* **2015**, *3*, 14942–14962.

[43] S. A. Francis, J. M. Velazquez, I. M. Ferrer, D. A. Torelli, D. Guevarra, M. T. McDowell, K. Sun, X. Zhou, F. H. Saadi, J. John, et al., *Chemistry of Materials* **2018**, *30*, 4902–4908.

[44] M. Asadi, B. Kumar, A. Behranginia, B. A. Rosen, A. Baskin, N. Repnin, D. Pisasale, P. Phillips, W. Zhu, R. Haasch, et al., *Nature communications* **2014**, *5*, 1–8.

[45] X. Hong, K. Chan, C. Tsai, J. K. Nørskov, *Acs Catalysis* **2016**, *6*, 4428–4437.

[46] Y. Xie, X. Li, Y. Wang, B. Li, L. Yang, N. Zhao, M. Liu, X. Wang, Y. Yu, J.-M. Liu, *Applied Surface Science* **2020**, *499*, 143964.

[47] P. Abbasi, M. Asadi, C. Liu, S. Sharifi-Asl, B. Sayahpour, A. Behranginia, P. Zapol, R. Shahbazian-Yassar, L. A. Curtiss, A. Salehi-Khojin, *ACS nano* **2017**, *11*, 453–460.

[48] X. Duan, C. Wang, A. Pan, R. Yu, X. Duan, *Chemical Society Reviews* **2015**, *44*, 8859–8876.

[49] M. S. Whittingham, *Intercalation chemistry* **1982**, 1–18.

[50] M. S. Whittingham, *Science* **1976**, *192*, 1126–1127.

[51] C. Chu, C.-F. Fu, P. Zhang, T. Pan, X. Ai, Y. Wu, P. Cui, Q. Huang, J. Ran, *Journal of Membrane Science* **2020**, *615*, 118520.

[52] J. Zou, F. Li, M. A. Bissett, F. Kim, L. J. Hardwick, *Electrochimica Acta* **2020**, *331*, 135284.

[53] X.-L. Li, Y.-D. Li, *The Journal of Physical Chemistry B* **2004**, *108*, 13893–13900.

[54] N. H. Attanayake, A. C. Thenuwara, A. Patra, Y. V. Aulin, T. M. Tran, H. Chakraborty, E. Borguet, M. L. Klein, J. P. Perdew, D. R. Strongin, *ACS Energy Letters* **2017**, *3*, 7–13.

[55] H. Zittel, F. Miller, *Analytical Chemistry* **1965**, *37*, 200–203.

[56] P. T. Kissinger, W. R. Heineman, *Journal of chemical education* **1983**, *60*, 702.

[57] N. Elgrishi, K. J. Rountree, B. D. McCarthy, E. S. Rountree, T. T. Eisenhart, J. L. Dempsey, *Journal of chemical education* **2018**, *95*, 197–206.

[58] C. Horwood in *Ionic Liquids in Analytical Chemistry*, Elsevier, **2022**, pp. 329–342.

[59] A. M. Pinto, V. S. Oliveira, D. S. C. Falcão, *Direct alcohol fuel cells for portable applications: fundamentals, engineering and advances*, Academic Press, **2018**.

[60] Z. Stojek in *Electroanalytical methods*, Springer, **2010**, pp. 3–9.

[61] K. D. Bartle, P. Myers, *TrAC Trends in Analytical Chemistry* **2002**, *21*, 547–557.

[62] W. Jennings, E. Mittlefehldt, P. Stremple, *Analytical gas chromatography*, Academic Press, **1997**.

[63] M. Swartz, *Journal of Liquid Chromatography & Related Technologies* **2010**, *33*, 1130–1150.

[64] S. Ebnesajjad in *Handbook of adhesives and surface preparation*, Elsevier, **2011**, pp. 31–48.

[65] S. K. Sharma, D. S. Verma, L. U. Khan, S. Kumar, S. B. Khan, *Handbook of materials characterization*, Springer, **2018**.

[66] D. E. Newbury*, N. W. Ritchie, *Scanning* **2013**, *35*, 141–168.

[67] J. C. Russ, *Fundamentals of energy dispersive X-ray analysis: Butterworths monographs in materials*, Butterworth-Heinemann, **2013**.

[68] H. Khan, A. S. Yerramilli, A. D'Oliveira, T. L. Alford, D. C. Boffito, G. S. Patience, *The Canadian journal of chemical engineering* **2020**, *98*, 1255–1266.

[69] D. Faggion Jr, W. D. Gonçalves, J. Dupont, *Frontiers in Chemistry* **2019**, *7*, 102.

[70] J. Chastain, R. C. King Jr, *Perkin-Elmer Corporation* **1992**, *40*, 221.

[71] S. Deng, M. Luo, C. Ai, Y. Zhang, B. Liu, L. Huang, Z. Jiang, Q. Zhang, L. Gu, S. Lin, et al., *Angewandte Chemie International Edition* **2019**, *58*, 16289–16296.

[72] K. D. Rasamani, F. Alimohammadi, Y. Sun, *Materials Today* **2017**, *20*, 83–91.

7

Appendix

7.1. CV results

The electrochemical Ca^{2+} intercalation was first studied by CV with 1 mM $CaCl_2$ as electrolyte. In order to better find the potential range, very slow scan rates are used (5 mV/s). The results are shown in Figure 7.2. Three experiments showed similar results. Charge transfer occurs during intercalation process, it should be reflected in the form of redox peaks In the figure. In the range of -2.1 V to -2.6 V vs SCE, a small redox peak appears. It can be speculated that intercalation can occur within this potential range.

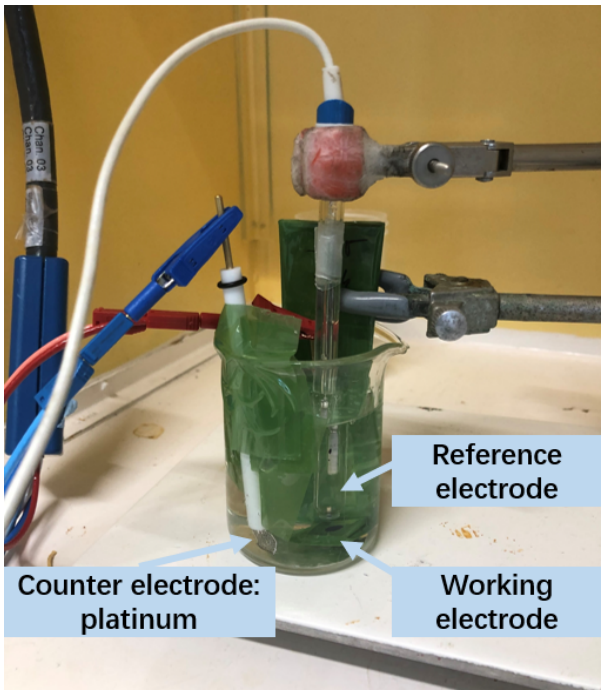

Figure 7.1: The setup for CV, LSV, CA, and EIS experiments.

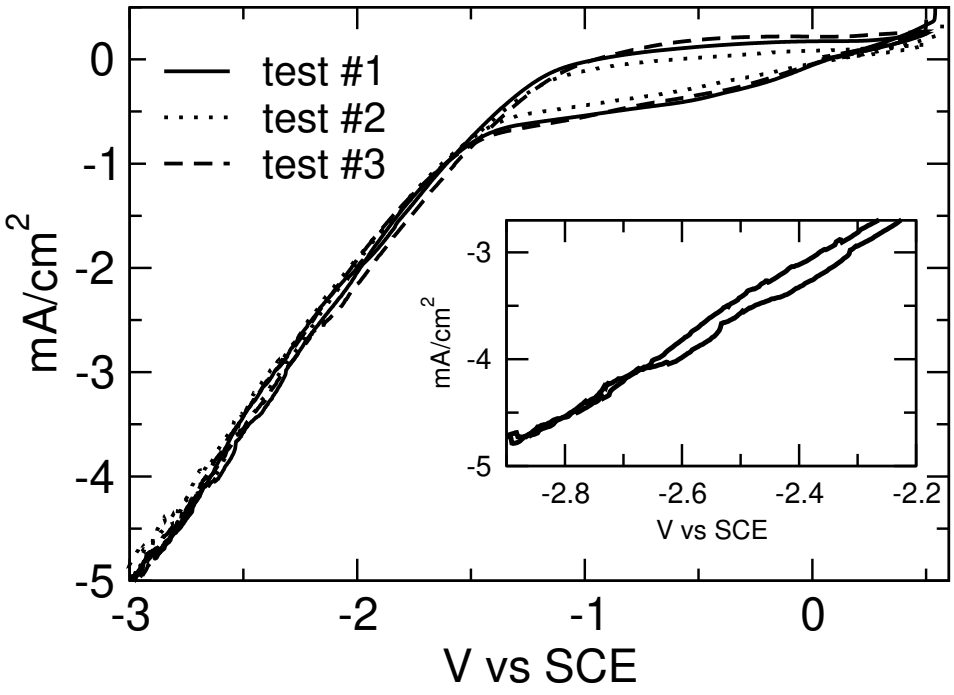

Figure 7.2: CV results of working electrode in 1 mM $CaCl_2$ solution. The potential range is from -3 V to 0.5 V. The small figure lists the result of test 1 separately.

7.2. EIS results

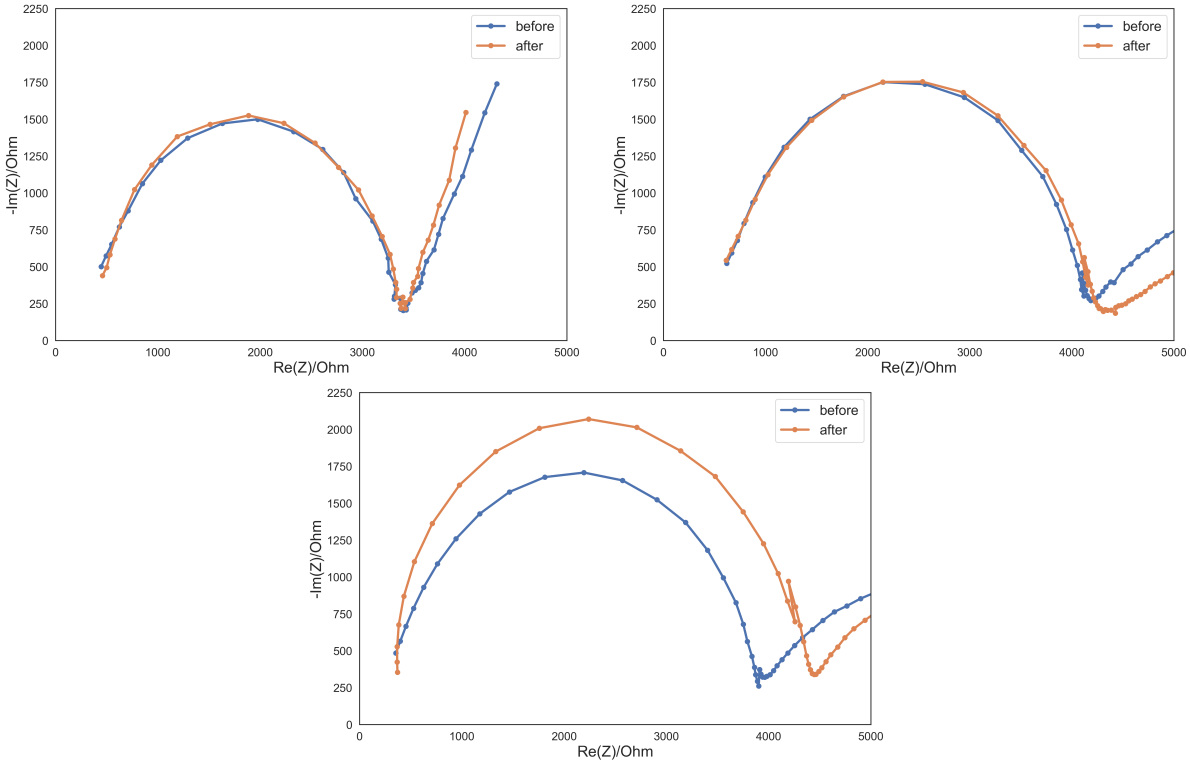

Figure 7.3: EIS test results in 1 mM $CaCl_2$ solution, the potential is (a) -2.1 V, (b) -2.2 V, and (c) -2.4 V vs Ag/AgCl.

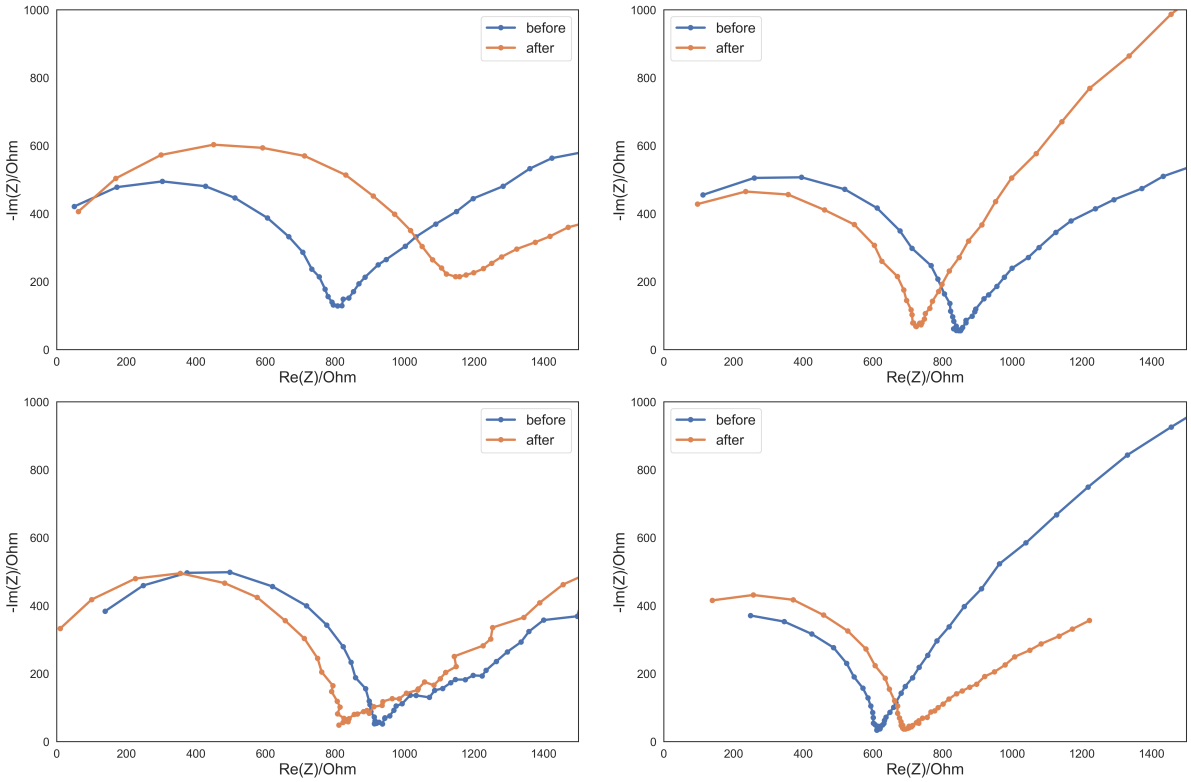

Figure 7.4: EIS test results in 5 mM $CaCl_2$ solution, the potential is (a) -2.0 V, (b) -2.1 V, (c) -2.2 V, and (d) -2.4 V vs Ag/AgCl

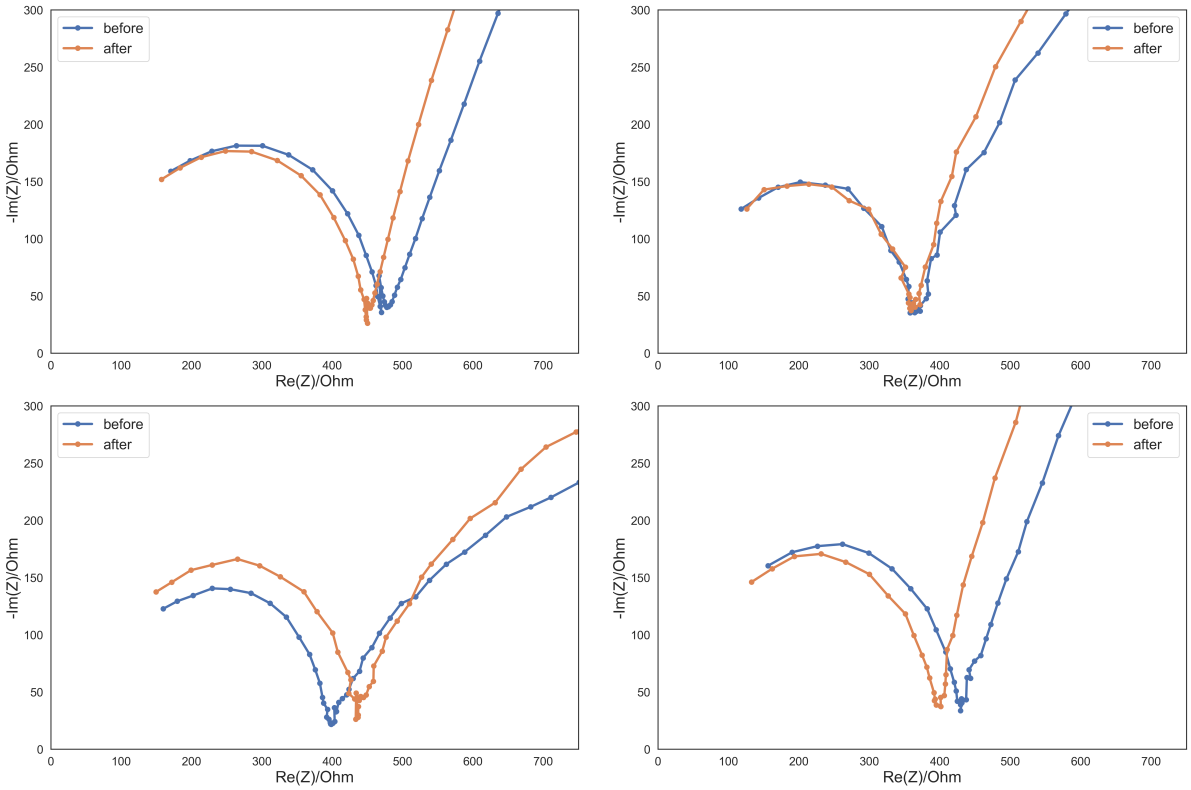

Figure 7.5: EIS tests results in 10 mM $CaCl_2$ solution, the potential is (a) -2.0 V, (b) -2.1 V, (c) -2.3 V, and (d) -2.4 V

7.3. GC

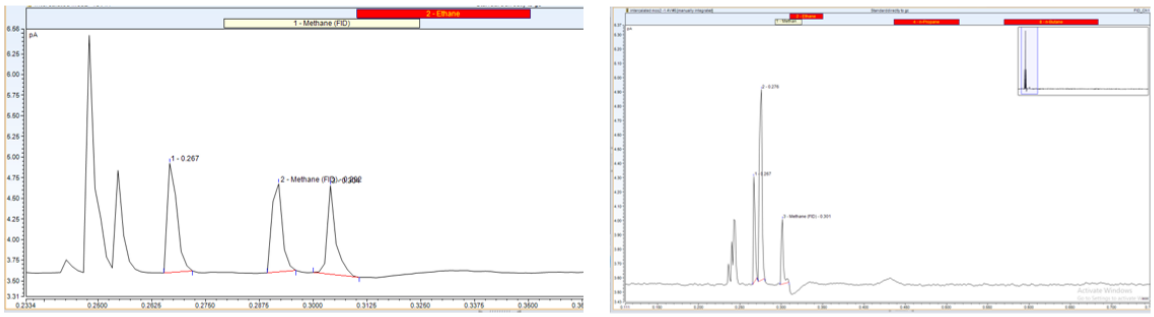

Figure 7.6: FID chromatogram.

7.4. NMR

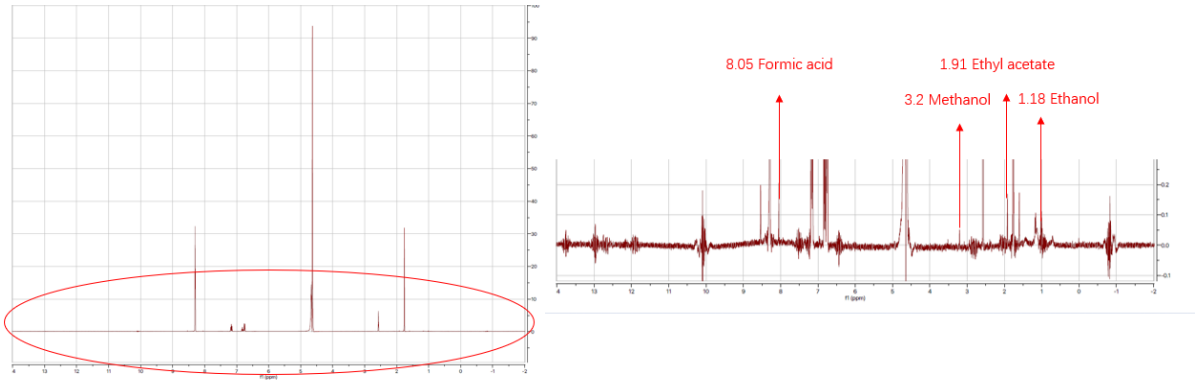

Figure 7.7: NMR spectra for intercalated MoS_2 sample at the potential of -1.5 V sv SCE.

7.5. EDS results

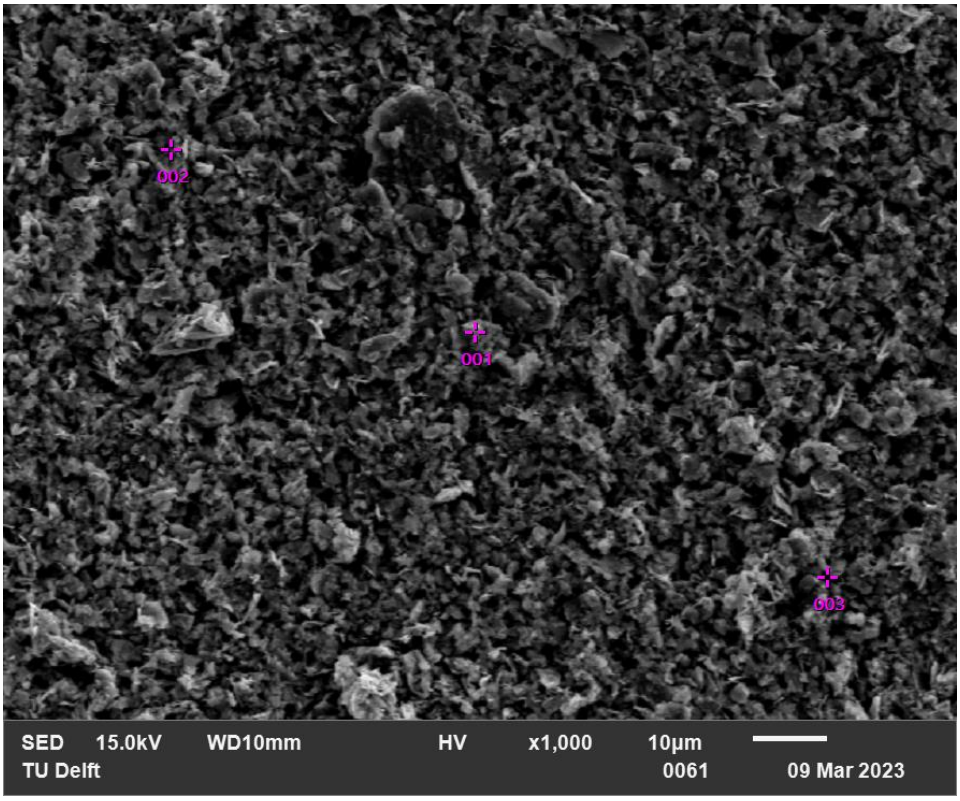

Figure 7.8: EDS points analysis of pristine MoS_2 sample.

Table 7.1: EDS points analysis of pristine MoS_2 sample

	Point 1		Point 2		Point 3	
Element	**Mass%**	**Atom%**	**Mass%**	**Atom%**	**Mass%**	**Atom%**
C	3.53	15.31	2.15	9.89	1.03	4.95
O	0.08	0.25	0	0	0	0
S	0.25	48.71	29.50	50.78	29.77	53.50
Mo	66.75	36.26	68.35	39.33	69.19	41.55
Total	100	100	100	100	100	100

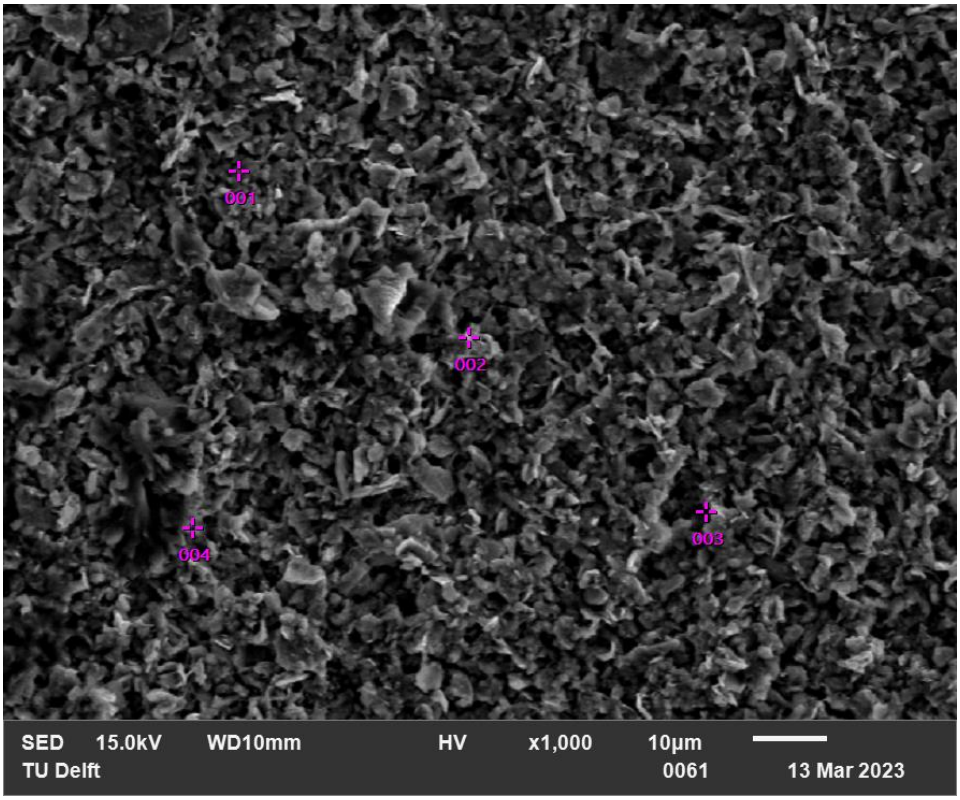

Figure 7.9: EDS points analysis of Ca^{2+} intercalated MoS_2 sample.

Table 7.2: EDS points analysis of Ca^{2+} intercalated MoS_2 sample

	Point 1		**Point 2**		**Point 3**		**Point 4**	
Element	**Mass%**	**Atom%**	**Mass%**	**Atom%**	**Mass%**	**Atom%**	**Mass%**	**Atom%**
C	13.77	34.46	16.44	39.83	12.82	34.72	7.12	22.26
O	15.70	29.49	14.35	26.09	11.19	22.76	8.82	20.71
S	18.85	17.66	19.22	17.44	21.97	22.29	23.48	27.51
Mo	46.66	14.62	46.52	14.11	49.97	16.95	10.59	9.93
Ca	5.02	3.76	3.47	2.52	4.04	3.28	50.00	19.58
Total	100	100	100	100	100	100	100	100

7.6. XPS results

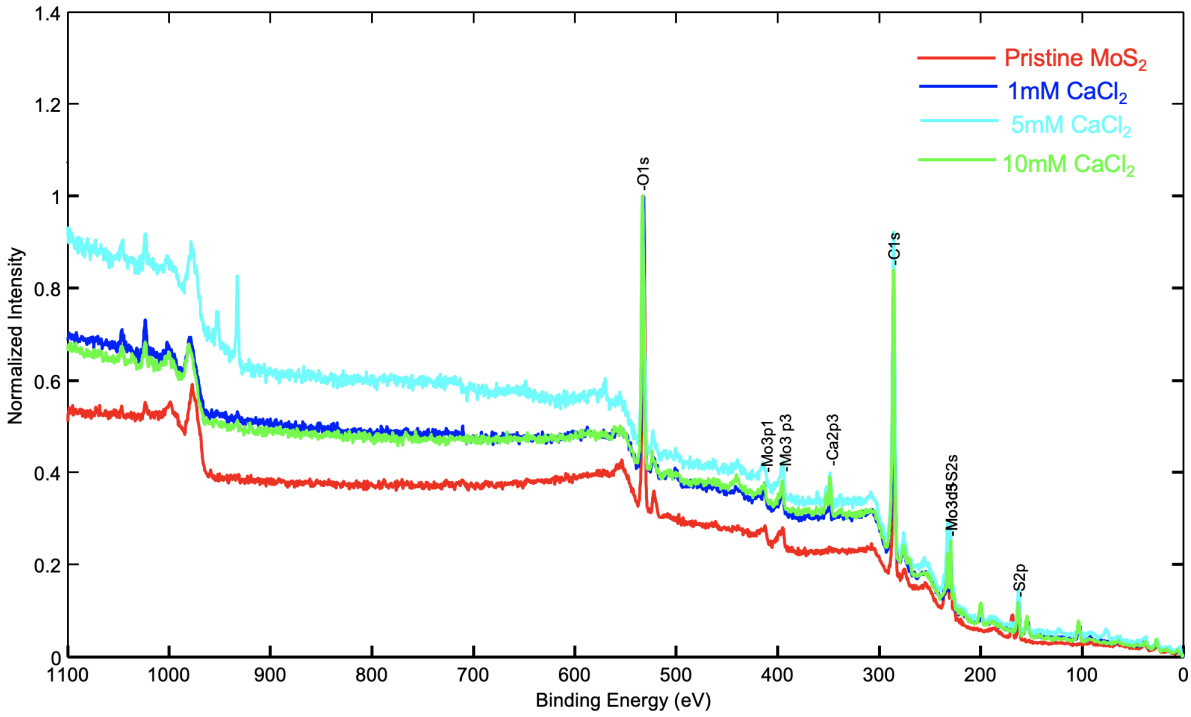

Figure 7.10: XPS spectra for MoS_2 and MoS_2 treated with 1 mM, 5 mM, and 10 mM of $CaCl_2$ solution.